

# Chapter 5

## Microwave-Processed Copper Zinc Tin Sulphide (CZTS) Inks for Coatings in Solar Cells

Prashant R. Ghediya and Tapas K. Chaudhuri

### 5.1 Introduction

Solar electricity, generated from sunlight by solar cells, is environmentally clean, carbon-free and renewable. It has the potential to meet the terawatt energy demand of the world, provided it is available at par with grid electricity. The prevalent solar cells made from silicon (Si) or cadmium telluride (CdTe) or copper indium gallium selenide (CIGS) generate electricity that are still too expensive. Hence, there is a frantic search for new materials for solar cells which will generate cost-competitive electricity [1]. One such promising candidate is earth-abundant, low-cost and non-toxic kesterite copper zinc tin sulphide/selenide. Copper zinc tin sulphide (CZTS) is a *p*-type semiconductor with a direct band gap of about 1.5 eV and absorption coefficient of above  $10^4 \text{ cm}^{-1}$  in the solar spectrum [2]. CZTS exists in tetragonal kesterite structure with lattice constants:  $a = 0.5435 \text{ nm}$ ,  $c = 1.0843 \text{ nm}$ . The absorber layer is the heart of TFSCs. The CZTS film in a thin film solar cell (photovoltaic device) acts as the *p*-type photoactive absorber layer. The absorber layer is the most critical part of a cell because major processes required for photovoltaic effect occur here. The processes of absorption of solar radiation, generation of electron-hole pairs and separation of charges take place in this layer. Hence, effect of light on conductivity (photoconductivity) of CZTS films is as important as the dark conductivity itself. In other words, understanding of electrical and photoelectrical properties of CZTS is essential for development of

---

P.R. Ghediya (✉)

Department of Physics, Faculty of Sciences, Marwadi University, Rajkot-Morbi Highway,  
Rajkot, Gujarat 360003, India  
e-mail: [prashantghediya@gmail.com](mailto:prashantghediya@gmail.com)

T.K. Chaudhuri

Department of Applied Physics, S. V. National Institute of Technology, Surat 395007, India

**Table 5.1** Suitability of CZTS as an absorber layer for solar cells [3]

Properties of absorber	Desirable	CZTS
Band gap	1–1.7 eV, direct transition	1.4–1.5 eV
Absorption coefficient	$10^4$ – $10^5$ cm <sup>-1</sup>	$>10^4$
Conduction type	<i>p</i> -type ( $10^{16}$ – $10^{17}$ cm <sup>-3</sup> )	<i>p</i> -type( $10^{15}$ – $10^{18}$ cm <sup>-3</sup> )
Mobility	High	High
Diffusion length of minority carriers	$> 1$ $\mu$ m	–
Availability	Abundant at affordable price	Earth-abundant
Toxicity	Non-toxic	Environmental benign
Deposition	Simple and amenable to large scale	Solution-processed

efficient solar cells. Table 5.1 confirms that properties of CZTS match quite well with the desired one.

Band gap of the absorber should be small enough to allow absorption of a significant portion of solar spectrum and at the same time large enough to minimize the reverse saturation current density. Direct band gap semiconductors (1–1.7 eV) with high absorption coefficient are preferred for this purpose [3]. Further, the diffusion length of the minority carriers must be large enough so that the generated carriers can reach the contacts without much loss. Therefore, in general, *p*-type semiconductors are used as absorber layers.

The intrinsic *p*-type conductivity, due to Cu-on-Zn antisites (Cu<sub>Zn</sub>), also makes it an ideal absorber material in solar cells due to the fast transfer of photo-generated holes at the front of illuminated side [4]. However, due to the formation of different binary and ternary secondary phases along with CZTS and various types of defects, achieving pure CZTS is rather difficult. Hence, different properties of CZTS including structural, compositional, optical, electrical and photovoltaic have been extensively studied. Variety of vacuum and non-vacuum deposition methods have been developed to fabricate efficient CZTS solar cells. However, CZTS solar cells fabricated from *direct ink coating* (DIC) technique have yielded, so far, efficiencies between 10 and 12.7% [5–7]. A numbers of reasons why we restrict to such technique have been elaborated below:

- Ink can be directly deposited on any types of substrate under any mild conditions.
- The present approach allows all advantages of non-vacuum deposition, like the possibility to use low-cost and high-throughput equipment, low wastage of raw materials and high uniformity of coated layer.
- Inks can be sprayed, screen-printed, ink-jet printed or doctor bladed via single deposition step which is ultimately implemented in a roll-to-roll industrial process.

Figure 5.1 shows the methodology to prepare different types of CZTS ink along with the deposition methods to prepare films. It may be noted here that efficiency of

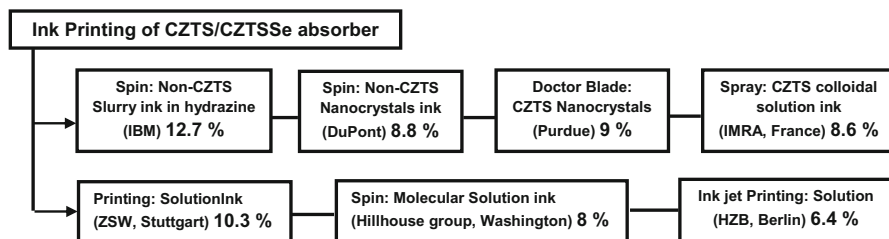


**Fig. 5.1** Different types of CZTS ink and printing methods to prepare films

12.7% was reported in August 2014 using hydrazine and there has been no improvement so far, even after 2 years! However, hydrazine is highly toxic and very unstable that requires extreme caution during handling. Hence, there is a need to replace these solvents by non-toxic solvents for preparation of CZTS inks. The synthesis of CZTS inks has been quite complex with time-consuming cumbersome procedures. Hence, there is a need for simple rapid process for making CZTS nanoparticle ink. Microwave-assisted [8] preparation methods have those capabilities.

## 5.2 Inks for Coatings

Figure 5.2 shows the various types of CZTS inks with their respective preparation methods. CZTS ink may be either a pure solution, i.e. metal salts dissolved in precursor solution, or suspension. The suspended particles can be synthesized with high purity, but the synthetic processes involve multiple steps, hence found tedious. On the other hand, molecular solution inks are stable. However, the later approach is less suited for the removal of excess organic solvents and precursors, mainly carbon.

On the other hand, CZTS inks can be synthesized either by mixing binary and ternary compounds such as  $\text{Cu}_2\text{S}$ ,  $\text{ZnS}$  and  $\text{SnS}$  in some solvents/capping or by dissolving pure metal salts directly in solvents. However, CZTS nanoparticle ink via suspension route seems to be more promising since it involves only a single step. For large-scale ink-based deposition of CZTS films, it is imperative that formulation of ink should be simple and straight forward preferably containing CZTS only. CZTS ink with suspended particles can be synthesized by hot-injection [9, 10], sonochemical [11], solvothermal [12] and microwave-assisted (MA) [8] methods. It was previously showed that the slurry-ink containing of molecular solution and non-CZTS NPs in toxic hydrazine yields best CZTSSe solar cells till date [6]. Figure 5.3 shows the cross-sectional scanning electron microscopy view and J-V characteristics of a champion CZTSSe device with the absorber layer produced by a non-vacuum solution/ink approach that uses hydrazine [7]. Hydrazine is a powerful reducing agent that, in presence of excess chalcogen

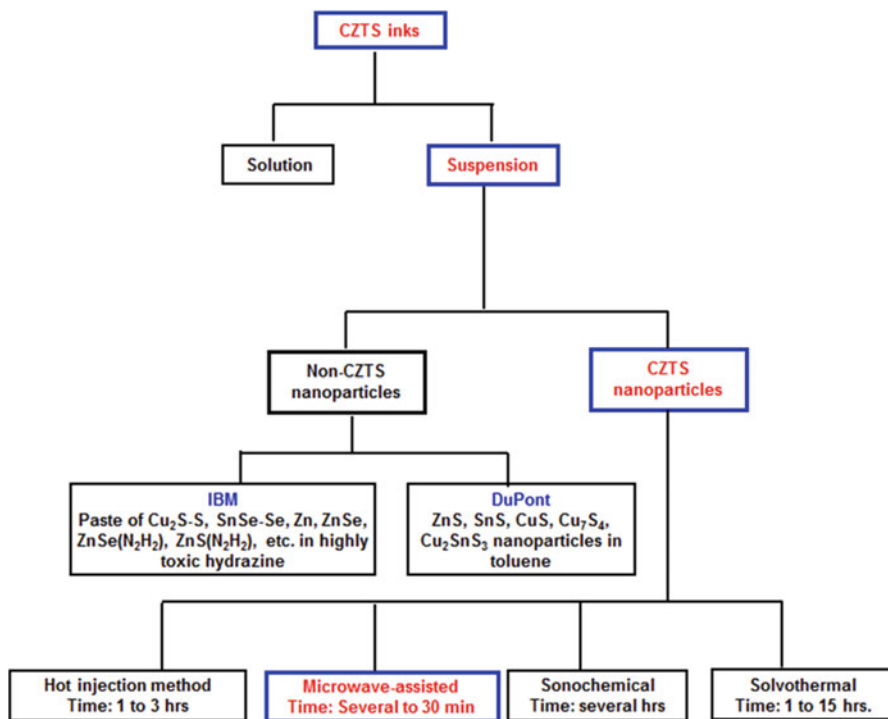


Fig. 5.2 Methodology for the preparation of CZTS inks

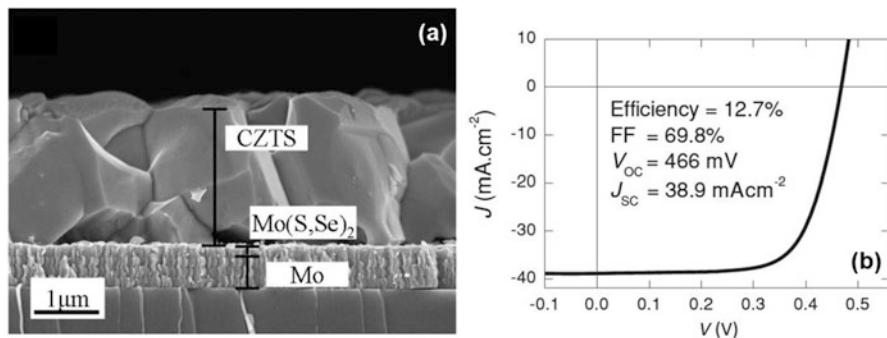


Fig. 5.3 (a) Cross-sectional SEM of the most efficient CZTSSe absorber and (b) J-V characteristics of the champion device [7]

(S, Se, Te), can solvate different metal chalcogenides as hydrazinium-based complexes at room temperature. Its controlled degradation produces N<sub>2</sub> and H<sub>2</sub> only, which are gaseous products that are released during thermal treatment and thus should not leave any contaminant in the CZTSSe film [13]. Because of its high toxicity and flammability, finding alternatives with a high solvating power,

reducing capability and ‘clean’ products upon degradation is highly desirable. Hence, there is a need to replace these solvents by non-toxic solvents for preparation of CZTS inks.

### 5.2.1 CZTS Nanoparticles Ink

CZTS nanoparticles (NPs) through hot-injection method were synthesized by Riha et al. [9] for the first time in 2009 and recently there has been significant interest both in CZTS and CZTSe NPs [14, 15]. The CZTS NPs have primarily been synthesized by hot-injection and solvothermal methods, where oleylamine (OLA) is often used as a solvent/surfactant/capping agent. Hot-injection method, in general, involves injecting a cold solution of precursors into a hot surfactant solution, thus leading to the instant nucleation and growth of nanocrystals. Table 5.2 presents the summary of CZTS NPs ink prepared by different methods.

At the same time, Guo et al. [10] investigated CZTS nano ink for solar cells by the same method. For making thin films, the CZTS inks were directly deposited on Mo-coated glass substrates by drop casting. The films were first annealed at 632 K for 1 h in argon atmosphere to remove the organic ligands. Finally, these films were selenized at 673–773 K under Se vapour in a graphite box to form CZTSSe absorber layer. The solar cells based on CZTSSe absorber yield efficiency of 0.80%. Similarly, Steinhagen et al. [16] also developed CZTS NPs ink for solar cells using OLA. However, the process varies from the others in the way that all precursors are mixed at room temperature (RT) in OLA and then heated to 553 K. It can be seen that all the above three groups have used OLA as a capping.

The NPs were generally synthesized using organic capping ligands for controlling the formation and growth. It provides good dispersibility in solvents enabling the formation of nanocrystal inks that can be deposited on substrates under mild conditions using direct ink coating methods. However, major problem with capping ligands is that they can hinder the charge transport in the nanocrystalline films. Complete removal of the ligands also leads to surface defects that trap electrons and holes which ultimately degrade the performance of solar photovoltaic devices [17].

Following these three groups [9, 10, 16], various researchers synthesized CZTS inks for low-cost solar cells by either changing the compositions of the metal salts or capping agents or source of sulphur. However, this process is not only complex but also time-consuming. It should be noted that OLA is hydrophobic and can only be dispersed into toluene which is also harmful.

Alternatively, CZTS NPs have been synthesized by solvothermal process [12, 18, 19]. Cao et al. [12] reported kesterite quaternary CZTS NPs by solvothermal process. In a typical process, appropriate amounts of copper chloride, zinc acetate, tin chloride and sulphur were added into a stainless steel autoclave with a Teflon liner, which was filled with ethylenediamine (EDA) up to 85% of the total volume (20 mL). The autoclave was sealed and maintained at 453 K for 15 h and then allowed to cool to RT naturally. The precipitates were filtered off, washed

**Table 5.2** Summary of CZTS nanoparticle ink prepared by different methods

Sr. No.	Author	Precursors	Preparation method	Solvents/capping	Temperature	Total time	Results
1	Riha et al. [9]	Cu(OAc) <sub>2</sub> + Zn(OAc) <sub>2</sub> + SnCl <sub>4</sub> + S	<b>Hot injection</b>	OLA + TOPO	423 K in vacuum for 30 min	3 h	Particle size = 12.8 ± 1.8 nm E <sub>g</sub> = 1.5 eV
2	Guo et al. [10]	All acetates+ S	Hot injection	OLA + toluene+ isopropanol	403 K in vacuum and degassed for 30 min	1 h	Particle size = 15–25-nm E <sub>g</sub> = 1.5 eV Efficiency(η) = 0.80%
3	Steinhagen et al. [16]	Cu(OAc) <sub>2</sub> + Zn(OAc) <sub>2</sub> + SnCl <sub>4</sub> + S	Hot injection	OLA	553 K in inert atm. for 1 h	1 h	Particle size = 10.6 ± 2.9 nm E <sub>g</sub> = 1.3 eV Efficiency(η) = 0.23%
4	Kameyama et al. [17]	All acetates + S	Hot injection	OLA	393–573 K in N <sub>2</sub> atm. for 60 min	1 h	Particle size = 5–6 nm E <sub>g</sub> = 1.5 eV
5	Cao et al. [12]	CuCl <sub>2</sub> + Zn(OAc) <sub>2</sub> + SnCl <sub>4</sub> + S	<b>Solvothermal</b>	EDA	453 K for 15 h	15 h	Particle size = 5–10 nm E <sub>g</sub> = 1.5 eV
6	Zhou et al. [18]	All chlorides + TU	Solvothermal	EG + PVP	503 K for 24 h	24 h	Particle size = 100–150 nm E <sub>g</sub> = 1.48 eV
7	Zaberca et al. [19]	All chlorides + TU	Solvothermal	EG + ethanol + tetra methyl ammonium hydroxide	473 K for 16 h	16 h	XRD: Secondary phase
8	Flynn et al. [8]	All chlorides + TAA	<b>Microwave</b>	EG	463 K for 30 min	30 min	Particle size = 7.6 ± 2.1 nm E <sub>g</sub> = 1.5 eV Efficiency(η) = 0.25%

9	Yang et al. [20]	Cu(NO <sub>3</sub> ) <sub>2</sub> + Zn(NO <sub>3</sub> ) <sub>2</sub> + SnCl <sub>4</sub> + S	Microwave	OLA + chloroform + hexane	533 K for 30 min and annealed at 623 K for several hours in N <sub>2</sub> gas	30 min	Particle size = 10–15 nm E <sub>g</sub> = 1.6 eV
10	Kumar et al. [21]	All chlorides + TU	Microwave	EG	–	3 h	Particle size = 7 nm E <sub>g</sub> = 1.76 eV
11	Shin et al. [22]	Cu(OAc) <sub>2</sub> + Zn(OAc) <sub>2</sub> + SnCl <sub>2</sub> + C <sub>2</sub> H <sub>5</sub> NS + NH <sub>4</sub> OH	Microwave	Water	Sulphurized in N <sub>2</sub> (95%) + H <sub>2</sub> S (5%) at 823 K for 1 h	10 min	Particle size = 42.1 ± 23.7 nm E <sub>g</sub> = 1.5 eV
12	Wang et al. [23]	All acetates + TU + PVP	Microwave	EG	–	Several min	Particle size = 250–350 nm E <sub>g</sub> = 1.5 eV
13	Sarswat et al. [24]	All acetates + dodecanethiol	Microwave	OLA/EG	–	20 min	Particle size = 8–16 nm E <sub>g</sub> = 1.7 eV
14	Wang et al. [25]	All acetate + S	Microwave	OLA	538 K for 15 min	15 min	Particle size = 38.9 ± 5.8 nm E <sub>g</sub> = 1.5 eV Carrier concentration (n) = 1.56 × 10 <sup>16</sup> cm <sup>-3</sup> Mobility (μ <sub>h</sub> ) = 4.86 cm <sup>2</sup> /Vs
15	Knuston et al. [26]	Cu(OAc) <sub>2</sub> + Zn(OAc) <sub>2</sub> + SnCl <sub>2</sub> + TU	Microwave	EG + thioglycolic acid + octadecene	433 K for 10 min		CZTS thin films directly into ITO Film thickness = 1–3 μm
16	Zhao et al. [27]	All chlorides + TU	Microwave	EG + PVP	473 K for 10 min	1 h	Films directly on FTO Particle size = 200–300 nm

(continued)

**Table 5.2** (continued)

Sr. No.	Author	Precursors	Preparation method	Solvents/capping	Temperature	Total time	Results
17	W. Wang et al. [28]	Cu(NO <sub>3</sub> ) <sub>2</sub> + Zn(OAc) <sub>2</sub> + SnCl <sub>2</sub> + TAA	Ultrasound-assisted microwave	PEG	403–453 K for 10 min	8 h	XRD: CuS Raman: CTS E <sub>g</sub> = 1.58–2.24 eV
18	Lin et al. [29]	All acetates + TU	Microwave-Assisted solvothermal	EDA + water	433–513 K for 1 h	7 h	Particle size = 200–500 nm XRD and Raman: Cu <sub>2</sub> S
19	Martini et al. [30]	Cu(OAc) <sub>2</sub> + SnCl <sub>4</sub> + Zn(OAc) <sub>2</sub> + Na <sub>2</sub> S	Microwave	Water + HCl + 3-mercaptopoacetic acid + NH <sub>4</sub> OH + dodecanthiol + methyl-ethyl-ketone	–		Particle size = 3–5 nm E <sub>g</sub> = 1.4 eV

Bold part separates the individual techniques used to synthesised CZTS nanoparticle ink



with absolute ethanol. The CZTS thin films were fabricated by dip coating technique on silicon substrate. Finally, the nanocrystalline thin films were annealed in H<sub>2</sub>S (5%)/Ar mixed gasses. The band gap of the CZTS NPs was 1.5 eV.

Zaberca et al. [19] also prepared CZTS NPs by solvothermal method for low-cost solar cells without any surfactant. For making ink, the appropriate metal chloride salts with TU were dissolved in mixture of ethylene glycol (EG) and methyl ammonium hydroxide (TMAOH). The resulting solution is loaded into a 1000 mL Teflon-lined steel autoclave and transferred into an oven preheated to the desired temperature. The autoclave is maintained at 473 K for 16 h and then cooled to RT. The CZTS thin films were deposited by dip coating method which was finally selenized at 823 K for 1 h. The films synthesized by this route shows good electronic properties and low-defect concentrations. Similarly, sphere-like kesterite CZTS NPs synthesized by a facile solvothermal method has also been reported by Zhou et al. [18]. The CZTS NPs were synthesized using EG and polyvinylpyrrolidone (PVP). In general, this technique allows for the precise control over the size, shape distribution and crystallinity of NPs. However, total processing time to synthesize CZTS NPs is too high (hours/days), and hence an additional improvement for reduction in time will be certainly required.

The use of microwave heating, in the place of conventional heating, is an alternative approach to synthesizing CZTS NPs. Microwave-assisted (MA) method for preparing CZTS ink seems to be promising since it is rapid. Microwave-based method has been employed in synthesizing NPs such as TiO<sub>2</sub>, ZnO and many other inorganic materials including chalcopyrite NPs. Recently, MA synthesis of CZTS absorber material was carried out by various authors [8, 20–30]. Synthesis of CZTS NPs using microwave-assisted approach was first reported by Flynn et al. [8] in 2012 with total processing time of 30 min. The authors utilized metal chloride salt and TAA as precursors in EG to synthesize CZTS NPs ink in one pot. The CZTS ink is directly spin coated into Mo-coated glass substrates. The film was annealed at 673 K for 20 min in the presence of tin(II) sulphide and sulphur under nitrogen flow to avoid sulphur loss and phase separation. The solar cell fabricated using CZTS NPs delivered photo conversion efficiency of 0.25%.

Subsequently, there have been reports [20–30] on MA synthesis of CZTS NPs using either different solvents or salts or sulphur sources. Kumar et al. [21] have used chloride salts while metal acetates have been used by Shin et al. [22] and Sarswat and Free [24]. Alternatively, Wang et al. [25] have used salts of acetylacetonate. A combination of copper nitrate, zinc acetate and tin chloride was also utilized [23]. For microwave heating, choice of appropriate solvent is vital since solvent itself acquires heat. Solvents such as EG [8, 21, 24], water [22] and OLA [25] have been used. Different sulphur sources, such as TAA [8, 22], elemental sulphur [25] and TU [21, 23, 24], were used for synthesis of CZTS. In general, after synthesis, NPs were first centrifuged, filtered, washed and then dispersed in some other solvent to prepare CZTS ink. The sizes of NPs were typically in the range 7–8 nm [8, 21, 24]. Flynn et al. [8] and Sarswat and Free [24] also deposited CZTS films from their inks. Further, there have been some reports on MA synthesis of CZTS inks and films. CZTS films were directly

deposited on ITO by Knutson [26]. Recently, mass production of CZTS NPs by microwave heating was also reported by Martini et al. [30]. The microwave ink was prepared by dissolving copper acetate, zinc acetate, tin chloride and sodium sulphide in mixture of acetic acid and water.

A critical assessment of earlier work on MACZTS NPs revealed that most of the authors [21–23, 25, 31–33] have synthesized CZTS NPs from solutions that are similar in composition. However, only very few [8, 24] have ultimately formulated ink from CZTS NPs. Further, solvents used for preparation of CZTS inks were completely different from those used for synthesis of CZTS NPs. In general, CZTS NPs were separated from the microwave solvent, cleaned, dried and dispersed in another solvent [8, 21–25]. That is, preparation of CZTS ink by microwave heating is rather complicated because of multiple cumbersome steps. However, it should be straightforward for mass scale.

### 5.3 Microwave Processing of Inks

A microwave is a rapid one-step process which is nowadays used to synthesize almost all types of materials, including sulphides, metals, phosphates, oxides and halides. Microwave irradiation is a form of electromagnetic energy which falls at the lower frequency end within electromagnetic spectrum and it is defined in the frequency range of 0.3–300 GHz (wavelengths range from 0.01 to 1 m). The frequency 2.45 GHz is preferred out of four available frequencies for industrial, scientific or medical applications since it has the suitable penetration depth to deal with laboratory scale samples, and there are power sources available to produce microwaves at this particular frequency. Microwave heating is often considered as '*microwave dielectric heating*'. This process is depending on the ability of a specific material to absorb microwaves and exchange it into heat. The mechanisms of microwave heating could be classified broadly into two different categories, i.e. dipolar polarization and ionic conduction [34].

Presently, chemical mechanisms take place by one of the two ways: conventional heating or microwave heating. In conventional heating, solvents and reactants are slowly activated by a conventional external heat source such as oil bath or hot plates. Heat is driven into the substance, passing first through the walls of the vessel in order to reach the solvent and reactants. However, this process is very slow.

In contrast, microwave heating generates efficient internal heating (in-core volumetric heating) by direct coupling of microwave energy with the molecules (solvents, reagents, catalysts) that are present in the reaction mixture, resulting in rapid rise in temperature. Since this process is not depending upon thermal conductivity of the vessel materials, the result is an instantaneous localized superheating of anything that will react to either dipole polarization or ionic conduction. The main benefit of using microwave-processed organic as well as

inorganic synthesis is the shorter reaction time. The reaction rate is determined by the Arrhenius equation as follow:

$$k = Ae^{-E_a/RT} \quad (5.1)$$

where  $T$  is the absolute temperature that controls the kinetics of the reaction and  $E_a$  is the activation energy. Further, the ability of a substance to convert electromagnetic energy into heat at a given frequency and temperature is determined by its tan delta loss which is given by Eq. (5.2) as,

$$\tan \delta = \epsilon''/\epsilon' \quad (5.2)$$

Tangent delta or tan delta loss is the dissipation factor of the sample. The dielectric constant or relative permittivity ( $\epsilon'$ ) describes the ability of a dielectric material to store electrical potential energy under the effect of an electric field. Dielectric loss ( $\epsilon''$ ) represents the amount of input microwave energy that is lost to the sample by being dissipated as heat. Three main dielectric parameter, tan delta loss, dielectric constant and dielectric loss are all related to the ability of a solvent to absorb microwave energy. The loss factor (tan delta loss) for some common solvents along with its boiling point and viscosity is summarized in Table 5.3. The solvents should be such that it absorbs the microwave energy very quickly and converts it into heat. Depending upon dielectric loss of solvents, it is divided into three categories, i.e. high, low and medium absorber solvents. The high absorbing solvents are one that has dielectric losses greater than 14 [35].

The aim of the present investigation is to coat CZTS films by doctor blading from ink. Hence, synthesis of appropriate CZTS ink is critical and imperative. Inks for deposition of semiconductor are of two types, i.e. suspension and solution. Suspension type of ink consists of micro or nano particles of material (CZTS) suspended in a solvent. However, in case of solution ink, the precursor chemicals are dissolved in the solvent. After doctor blading, the film is obtained by evaporating the solvent and heating at higher temperatures to obtain the final film. In case of solution ink, CZTS precursor is dissolved in a solvent. After deposition of films, the wet layer is preheated to evaporate the solvent. The dry films which are the precursor layer is then heated at thermolysis temperature (473 K for CZTS) to thermochemically convert it to CZTS. The CZTS film is finally annealed at higher temperature to achieve large grains. However, the present investigation is only restricted to suspension inks. For preparation of suspension ink, microwave process has been used for rapid in situ synthesis of CZTS particles.

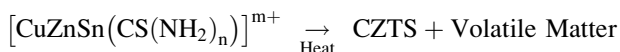
**Table 5.3** Different properties of most common solvents

Solvent	Boiling point (K)	Viscosity (cP)	Dielectric loss	Tan $\delta$ loss
Ethylene glycol	470	16.1	49.95	1.350
DMSO	462	1.99	37.12	0.825
Nitrobenzene	483	1.80	20.49	0.589

### 5.3.1 Basis for Development of CZTS Ink

One of the major objectives of this investigation is to prepare CZTS nanoparticle ink by microwave processing. The desired suspension ink essentially consists of nanoparticles of kesterite CZTS homogeneously dispersed in a solvent. Microwave processing as described above is not only simple and rapid but also does not require complicated experimental arrangement. The idea is to prepare CZTS suspension ink by microwave heating of a solution consisting of CZTS precursor dissolved in an appropriate solvent without any capping agent. Hence, the choice of CZTS precursor and solvent is important.

It has been observed by Chaudhuri and Tiwari [36] of our group that a complex of  $\text{Cu}^+$ ,  $\text{Zn}^{++}$ ,  $\text{Sn}^{++}$  and thiourea (CZTTU) is an excellent CZTS precursor and thermolyze to kesterite CZTS at around 473 K as depicted by the reaction:



The thermogravimetric analysis (TGA) of the dry complex powder is shown in Fig. 5.4. The graph reveals that the CZTTU complex starts decomposing at around 473 K. The CZTTU solution was prepared by dissolving copper (II) acetate (0.1 mol/L), zinc acetate (0.05 mol/L), tin (II) chloride (0.05 mol/L) and thiourea (0.5 mol/L) in methanol acidified by a few drops of HCl.

In the compound  $\text{Cu}_2\text{ZnSnS}_4$ , copper is in  $\text{Cu(I)}^+$  state while tin is in  $\text{Sn(II)}^{++}$  state. Although the starting salt of copper in solution is  $\text{Cu(II)}^{++}$ , under acidic condition TU reduces  $\text{Cu(II)}^{++}$  to  $\text{Cu(I)}^+$  by forming stable  $[\text{Cu}(\text{TU})_3]^+$  complex

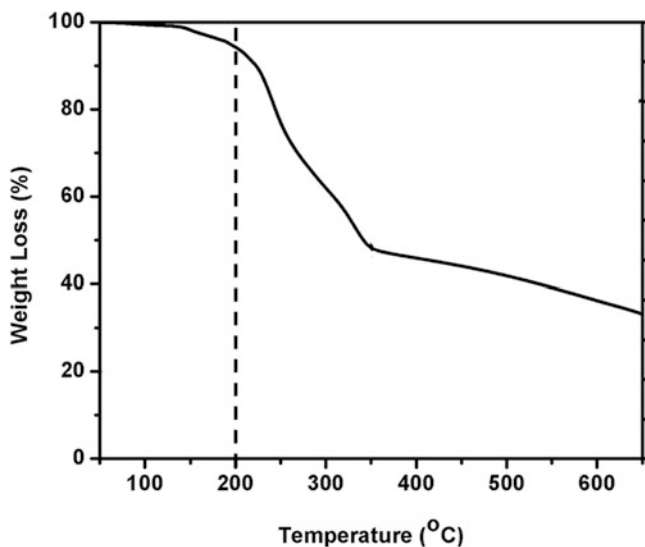
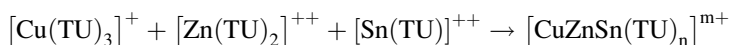


Fig. 5.4 Thermogravimetric analysis of metal-thiourea complex precursor

[37]. TU also readily forms soluble complexes with  $Zn^{++}$  and  $Sn^{++}$  as  $[Zn(TU)_2]^{++}$  and  $[Sn(TU)]^{++}$ , respectively. When all these TU complexes are mixed in methanol, the CZTS precursor (CZTTU) is produced, given by the reaction:



Hence CZTTU complex, suggested by Chaudhuri and Tiwari [36], was used as a CZTS precursor for synthesis of ink by microwave heating. The selection of appropriate solvent for ink was very vital. The ultimate solvent had to meet the following criteria:

- Precursor chemicals should dissolve easily
- Boiling point should be around 473 K
- Should be favourable to microwave heating, that is, high  $\tan\delta$  loss
- Should have moderate viscosity for doctor blading

Some of the common solvents with boiling point  $\sim 473$  K are listed in Table 5.3.

It can be seen that ethylene glycol (EG) qualifies as appropriate solvent for preparing ink since it has boiling point of 470 K, moderate viscosity of 16 cP and high  $\tan\delta$  loss of 1.35. Further, all the chemicals required for synthesis of CZTS precursor (CZTTU complex) are dissolved easily in EG. The basic concept of microwave synthesis of CZTS ink is as follows:

First, CZTS precursor (CZTTU) is dissolved in EG to form a clear solution. The solution is then heated with microwave radiation. During heating, EG rapidly attains temperature of 470 K and starts boiling. At this temperature ( $\sim 473$  K) CZTTU molecules present in EG also thermolyzes to CZTS, thus producing CZTS particles in situ EG.

To prove the above concept, CZTS powders were first synthesized in EG by microwave processing. This was followed by making of CZTS inks with micro and nano particles dispersed in EG. Molecular ink with CZTTU in EG and methanol was also prepared for comparison [38, 39].

Figure 5.5 reveals that a high microwave absorbing solvent EG ( $\tan\delta = 1.350$ ) can be rapidly superheated to temperatures  $> 473$  K above its boiling point when irradiated under suitable microwave conditions. Generally, this is difficult to achieve using standard thermal heating. During microwaving, the temperature of PS is rapidly ramped from 303 to 433 K in about 90 s at a heating rate of about  $5^\circ/s$ . There is no hold time. In short, the microwave is a type of rapid thermal processing.

### 5.3.2 Synthesis of Micropowder

CZTS powder was made from microparticle ink synthesized by microwave irradiation of precursor solution (PS) consisting of copper (II) acetate (0.1 M), zinc acetate (0.05 M), tin (II) chloride (0.05) and thiourea (0.5 M) in EG. All the

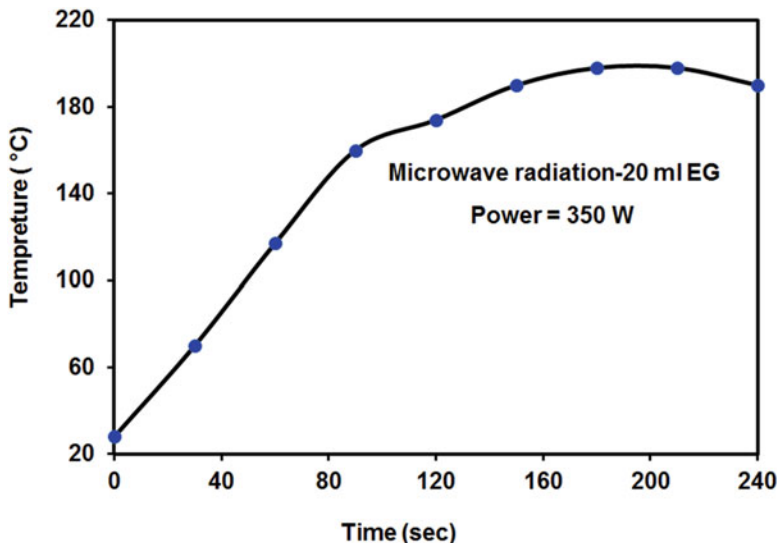


Fig. 5.5 The temperature increases of ethylene glycol (20 mL) at 350 W microwave power

chemicals and solvents used in the present work are of analytical grade supplied by Merck limited, India. Typically 100 mL of PS was heated in a domestic microwave oven for 5 min operated at 350 W. The temperature of the PS was instantly rose to 473 K, converting clear solution into black micro particles. The particles were separated from the ink by centrifugation at 8000 rpm for 10 min. The particles were cleaned and washed with methanol several times. Finally, the products were dried at 373 K in vacuum for several hours. The particles were then heated in a furnace at 473 K in air to remove any residual EG for few minutes. Upon heating, the particles are converted into black powders as shown in Fig. 5.6. The powder was then converted into pellet using steel dye and punch. For making pellets, the pressure of 10 ton was applied using hydraulic press. The diameter and height of the pellet was ~10 mm and 3 mm, respectively.

### 5.3.3 *Microparticle Ink*

Earlier section reveals that CZTTU precursor yields pure kesterite CZTS phase. However, to further explore the sulphur source, CZTS ink has been synthesized using six different sulphur sources. These are: thioglycolic acid (TA), sodium thiosulphate (ST), thiourea (TU), sodium sulphide (SS), sulphur (S) and thioacetamide (TAA). The precursor solution (PS) was prepared by dissolving copper (II) acetate (0.1 mol/L), zinc acetate (0.05 mol/L), tin (II) chloride (0.05 mol/L) and above sulphur sources (0.5 mol/L) step by step in separate beaker

**Fig. 5.6** CZTS micropowder after heating at 473 K in air

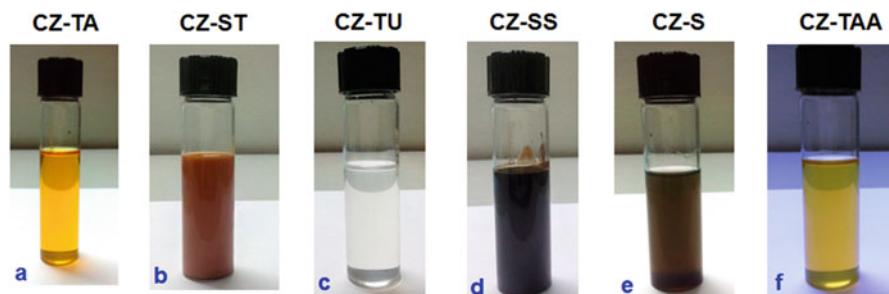


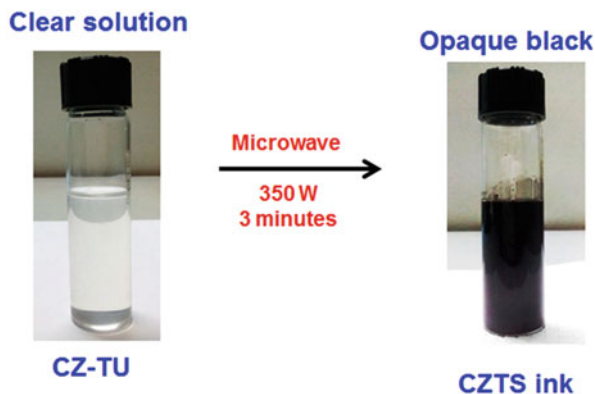
**Fig. 5.7** CZTS precursor solution synthesized in different sulphur sources: (a) thioglycolic acid (TA), (b) sodium thiosulphate (ST), (c) thiourea (TU), (d) sodium sulphide (SS), (e) sulphur (S) and (f) thioacetamide (TAA)

in 20 mL of EG. Figure 5.7 shows the CZTS precursor solution prepared using different sulphur sources.

It is also clear that TA-, TU- and TAA-based PS is clear. Further, only TU-based PS is clear and stable. Hence, it is confirmed that TU is suitable for making clear homogeneous solution. Further, CZTS ink was prepared using entire sulphur sources using microwave heating.

For the synthesis of ink, 20 mL of PS was placed in a domestic microwave oven operated at 350 W. In about 3 min, the temperature of the PS increased to 463 K and consequently the clear PS was converted into black opaque ink. The microwave production of CZTS ink in TU is depicted in Fig. 5.8. The similar procedure was done for all the sulphur sources. It is interesting to note that the ink was synthesized without adding any capping or legends unlike to those reported by Riha et al. [9] and Saraswat et al. [24].

**Fig. 5.8** Synthesis of microwave-processed microparticle CZTS ink



### 5.3.4 Nanoparticle Ink

CZTS microparticle ink has been synthesized by a one-step method involving the microwave heating of a glycolic solution of copper (II) acetate, zinc acetate, tin (II) chloride and thiourea. However, similar precursor solution of lower concentration, when irradiated with lower microwave power and longer duration, yielded CZTS nanoparticles (NPs).

In typical process, precursor solution was prepared by dissolving copper acetate (0.01 mol/L), zinc acetate (0.005 mol/L), tin chloride (0.005 mol/L) and thiourea (TU, 0.05 mol/L) as copper, zinc, tin and sulphur sources, respectively, in acidic EG. First, 20 mL of clear glycolic solution was microwaved at 250 W for 10 min. Within 10 min, a temperature of the solution was rose to 463 K, converting a clear solution into brown transparent stable ink. The ink was then allowed to cool naturally to the room temperature in air. The process of making CZTS NPs is shown in Fig. 5.9. This ink was used directly without any further treatments for the deposition of films.

Figure 5.9 shows that the clear colourless glycolic solution coating of meta-TU complex turned rapidly into clear brown CZTS ink upon microwave heating. During microwaving the temperature of the solution was rapidly increased to ~463 K, which is actually a boiling point of EG (460 K). It was showed in the earlier section that  $\text{Cu}^{+2}$ ,  $\text{Zn}^{+2}$ ,  $\text{Sn}^{+2}$  and TU form a complex which thermally decomposes to CZTS at ~463 K. Some volatile products were formed during thermolyses which escape into the air leaving only CZTS as a final product. In the present investigation  $\text{Cu}^{+2}$ ,  $\text{Zn}^{+2}$ ,  $\text{Sn}^{+2}$  and TU also form a complex in EG. During microwave irradiation, the complex thermolyzes to CZTS in situ the solvent EG. The other volatile products are expelled into the air. It was observed that during microwave heating, the precursor solution not only boiled but also copious bubbles were generated throughout the volume of the solution.



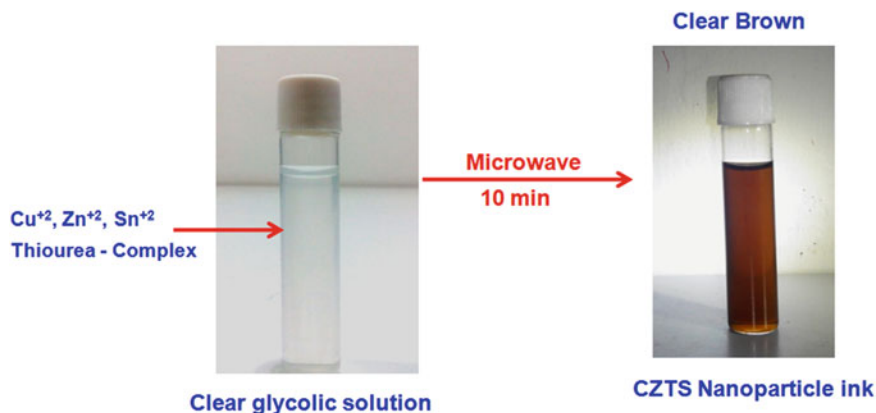


Fig. 5.9 Microwave-processed nanoparticle CZTS ink [40]

### 5.3.5 Characterizations

The synthesized products (inks/powder/films) have been characterized for structural, optical, morphological and electrical properties. The shapes and sizes of the CZTS nanoparticles were observed by a transmission electron microscope (TEM, Philips, Tecnai 20). A drop of ink was placed on a carbon-coated TEM grid and dried for observation under TEM. The transmittance spectrum of the nano inks was measured using an UV-VIS-NIR spectrophotometer (Shimadzu, UV-3600) in the wavelength range of 200–1500 nm. Band gap of CZTS powder has been measured in diffuse reflectance mode using integrating sphere. An X-ray diffractometer (Bruker, D2 PHASER) was used to identify CZTS with Ni-filtered  $\text{CuK}\alpha$  radiation ( $\lambda = 1.5418 \text{ \AA}$ ) operated in the  $2\theta$  range from 10 to  $80^\circ$ . The elemental composition of the films was analysed by energy dispersive X-ray spectroscopy (EDS Philips XL 30). Cross-sectional views of films were analysed by a field-emission scanning electron microscope (FE-SEM, Carl Zeiss 55). The thickness of the samples was also estimated from the cross-sectional SEM view. The vibrational modes of CZTS were analysed by a Laser Raman Spectrometer (LRS Jobin–Yvon, HR800) with an excitation wavelength of 514 nm in the range of 200–500 nm to identify the proper phase of the CZTS. The Raman spectra were calibrated by standard Si wafer (Raman shift of  $520 \text{ cm}^{-1}$ ). A linearly polarized Ar-ion laser beam with a power of 10 mW was focused into a spot size  $1 \mu\text{m}$  in diameter.

For the electrical measurements gap cells ( $\sim 2 \text{ mm}$ ) were fabricated with graphite paint (Ted Pella) as ohmic contacts. The films were dried under IR lamp at room temperature for few minutes. The electrical conductivity of the CZTS films in the temperature range of 77–500 K in the dark and under light were measured using cryostat (Janis VPF-100). The dark and photocurrent was measured with a source/meter unit (Keithly 2611) and a data acquisition system.

## 5.4 Issues in CZTS

A slight deviation from the optimal growth conditions (1–2%) will result in the formation of secondary phases, including ZnS,  $\text{Cu}_2\text{SnS}_3$  (CTS), SnS,  $\text{SnS}_2$  and CuS. The growth of these materials induced many problems in quaternary CZTS which ultimately affects the overall efficiencies. Chemical potential  $\mu_{\text{Sn}}-\mu_{\text{Zn}}$  diagram reveals only about 0.1 eV wide stability regions for Cu-rich CZTS compositions. The following sections describe the effect of some detrimental phases on final device and defects associated with it.

### 5.4.1 Detrimental Phases

Due to the complexity of the material and quaternary nature, the numbers of secondary phases are likely to form within CZTS. The most common ones are  $\text{Cu}_2\text{SnS}_3$  (CTS) and ZnS. A wide list of secondary compounds along with CZTS is reported in the literature. The secondary phases are detrimental for photovoltaic devices. Cu-S and Cu-Sn-S compounds are unfavourable for CZTS, being highly conductive phases [41], which can create shunting paths in the final devices. Table 5.4 shows the formation of possible secondary phases with their common properties.

CTS can form a solid solution with CZTS which lowers the  $E_g$  and ultimately increasing the conductivity of the final compound. On the other hand, copper sulphide phases appear in Cu-rich or Sn-poor conditions. They are low band gap semiconductors. Thus, they have a metallic behaviour, it means they can shunt the solar cells if their grains are big or in such a quantity that connects the front to the back electrode in the device. Small CuS/ $\text{Cu}_2\text{S}$  crystals act as traps for electrons and holes and enhance recombination. As far as transport properties are concerned, these phases are responsible for lowering the mobility and hence increase the carrier concentrations [43]. The effect of this phase on the final devices is still unclear as presence of ZnS was also observed in the best solar cells [44]. In general, these phases are responsible to suppress the overall efficiencies in CZTS thin films solar cells (TFSCs). Copper-poor, Zinc-rich compositions are therefore beneficial to suppress Cu-S phase and are generally taken in the literature for realization of high-efficiency CZTS devices [45].

Copper sulphide phases such as  $\text{Cu}_2\text{S}$ , CuS and unwanted phases based on tin (SnS,  $\text{SnS}_2$  and  $\text{Sn}_2\text{S}_3$ ) are easily detected by XRD as diffraction peaks of these phases and CZTS are completely different. However, due to the similarity in crystal structure and lattice constant of ZnS and CTS, these phases cannot be identified by XRD alone. Figure 5.10 shows the comparison of XRD patterns of kesterite CZTS along with CTS and ZnS. It is seen that the primary peaks of CZTS, CTS and ZnS are overlapping on each other and hence impossible to distinguish from XRD. Further, it has been shown that only 0.1% energy is required to phase separate

**Table 5.4** List of probable secondary phases observed in CZTS [42]

Materials	Crystal structure	Band gap	JCPDS	Type of semiconductor
$\text{Cu}_2\text{ZnSnS}_4$	Kesterite tetragonal	1.5	26-0575	P
$\text{Cu}_2\text{SnS}_3^{\text{a}}$	Cubic	0.96	89-2877	P
$\text{Cu}_2\text{SnS}_3^{\text{a}}$	Tetragonal	1.12	89-4714	P
$\text{Cu}_3\text{SnS}_4$	Orthorhombic	1.60	36-0218	P
$\text{Cu}_4\text{SnS}_6$	Rhombohedral	–	36-0053	P
$\text{ZnS}^{\text{a}}$	Sphalerite-Cubic	3.54	05-0566	Insulator
$2\text{H-ZnS}^{\text{a}}$	Wurtzite-Hexagonal	3.91	79-2204	Insulator
CuS	Covellite-Hexagonal	1.7	06-0464 75-2233	P
$\text{Cu}_2\text{S}^{\text{a}}$	Low-Chalcocite Orthorhombic	1.18	23-0961 73-1138	P
$\text{Cu}_2\text{S}^{\text{a}}$	High-Chalcocite Hexagonal	–	84-0206	P
$\text{Cu}_9\text{S}_5$	Digenite-rhombohedral	1.8	47-1748 84-1770	P
$\text{Cu}_7\text{S}_4$	Anilite-orthorhombic	–	72-0617	P
$\alpha\text{-SnS}$	Herzenbergite-orthorhombic	1.3	83-1758 (Amnm)	P
$\beta\text{-SnS}$	–	1.3	73-1859 (Pbnm)	P
$\text{SnS}_2$	Berndtite-Rhombohedral	2.2	23-0677 83-1705	N
$\text{Sn}_2\text{S}_3$	Orthorhombic	1.09	75-2183	N

<sup>a</sup>Most common observed phases in CZTS

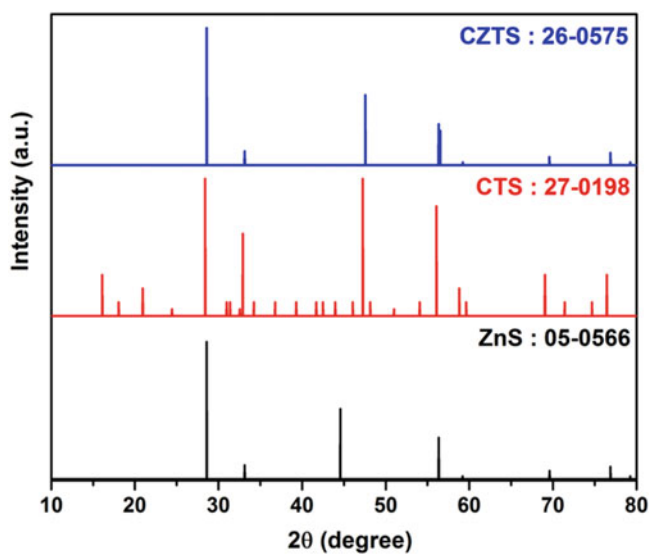


**Fig. 5.10** Powder X-ray diffraction patterns showing overlapping of kesterite CZTS with related secondary phases

**Table 5.5** Raman peaks of different binary and ternary compounds [49]

CZTS	Cu <sub>2</sub> SnS <sub>3</sub>	Cu <sub>3</sub> SnS <sub>4</sub>	Cu <sub>2</sub> S	ZnS	SnS <sub>2</sub>	SnS
266	–	295	264	278	–	164
288	295–303	318	–	–	–	192
338	355	348	–	351	315	218
368–374	–	–	475	–	–	–

stoichiometric CZTS into ZnS and CTS [46]. Experimentally, both ZnS and CTS have been scrutinized within CZTS, which can only be confirmed by Raman spectroscopy.

Raman spectroscopy is the precise technique used to studying the presence and spatial distribution of various chalcogenide and kesterite phases. Slight differences in the phonon densities of states between these phases can be easily distinguished from the shifts in Raman scattering peaks. Table 5.5 illustrates the peak position (Raman shift) of different binary and ternary sulphides along with CZTS. Further, Fernandes et al. [47], Fontane et al. [48] and Cheng et al. [49] used a 514 nm laser source in Raman spectroscopy to successfully identify and distinguish the presence of CTS, Cu<sub>3</sub>SnS<sub>4</sub>, Cu<sub>2</sub>S, ZnS and SnS<sub>2</sub> in CZTS. Hence, in the present work, the same source has been utilized to examine the CZTS samples.

Table 5.5 reveals that the Raman peaks of CZTS, CTS and ZnS are completely different. Himmrich and Haeuseler [50] studied the Raman spectra of CZTS and other stannite and wurtzstannite compounds. They identified a primary peak at 336 cm<sup>-1</sup> and two weaker peaks at 285 and 362 cm<sup>-1</sup>, for CZTS. Recently, a most intense peak of CZTS thin films has been found at 336–338 cm<sup>-1</sup> and the weaker peaks at 287–288 cm<sup>-1</sup> and 368–374 cm<sup>-1</sup> [14, 51, 52]. The primary peak of CZTS has been found to vary from 339 to 330 cm<sup>-1</sup> depending upon growth conditions [53, 54]. The distribution of Raman peaks in CZTS is explained by selection rules which can only be identified using polarization Raman study. The irreducible representation of the zone centre phonon mode in kesterite structure is given as [55].

$$\Gamma = 3A \oplus 6B \oplus 6E \quad (5.3)$$

The main peak in CZTS is dominated by the A1 vibrational mode. The weaker peak at 287 cm<sup>-1</sup> is due to the B symmetry mode corresponding to movements of the Cu/Zn and Cu/Sn atomic planes [55]. However, minor peak appearing in the range 350–380 cm<sup>-1</sup> is assigned to B and E symmetry mode of CZTS.

### 5.4.2 Defects

Crystal defects are inevitable in chalcopyrite and quaternary kesterite semiconductors and always associated with their photovoltaic properties. One of the major factors limiting the efficiency of TFSCs is the occurrence of different types of

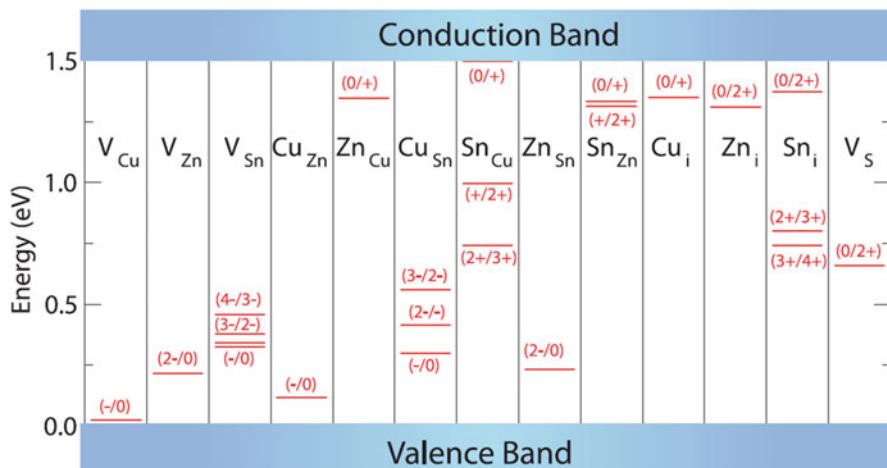


Fig. 5.11 The ionization levels of intrinsic defects in the band gap of CZTS [46]

defects, like vacancies, antisites, interstitials and clusters, which affect the charge transport mechanisms in the solar cells. Further, higher number of constituent atoms makes the properties of the intrinsic defects more intricated. Theoretical studies have predicted various intrinsic point defects including vacancies ( $V_{Cu}$ ,  $V_{Zn}$ ,  $V_{Sn}$  and  $V_S$ ), antisites ( $Cu_{Zn}$ ,  $Zn_{Cu}$ ,  $Cu_{Sn}$ ,  $Sn_{Cu}$ ,  $Zn_{Sn}$  and  $Sn_{Zn}$ ), interstitials ( $Cu_i$ ,  $Zn_i$  and  $Sn_i$ ) and several defect complexes may play crucial part in CZTS depending on its composition [56].

Crystal structural, electronic state and point defect formation of kesterites and chalcopyrites have been investigated using density functional theory (DFT) [56]. These examinations have revealed both similarities and differences between kesterites and chalcopyrites. Antisite defects can form either acceptor or donor levels in CZTS, subjected to their formation energies or transition levels. The ionization levels of various point defects were predicted by Chen et al. [56] as summarized in Fig. 5.11. The dominant  $p$ -type acceptor in kesterite CZTS is the  $Cu_{Zn}$  antisite defect.

According to Chen et al. [56], the  $V_{Cu}$  results in a shallow acceptor level just above the valence band, while the  $Cu_{Zn}$  antisite results in a level 0.12 eV higher in energy. Lowest formation energy is reported in  $Cu_{Zn}$  antisite by Chen et al. [57] whereas a negative value is also reported by Nagoya et al. [58]. However, calculations reported in [57] predict that the  $Cu_{Zn}$  formation energy becomes negative for Fermi level higher than 0.12 eV. In general, these investigations prevent the possibility of an  $n$ -type doping. Apart from the  $Cu_{Zn}$  antisites, other four dominant defects are expected, showing relatively low formation energy for Cu-poor CZTS compositions. These defects, in terms of increasing formation energy:  $V_{Cu}$ ,  $Zn_{Sn}$ ,  $V_{Zn}$  and  $Cu_{Sn}$ .

Formation of donor defects is rather unlikely due to the high formation energies or the facile formation of compensating acceptors [59]. The lowest formation energy was reported for the defect complex  $[\text{Cu}_{\text{Zn}} + \text{Zn}_{\text{Cu}}]$  [60] which give rise to the possibility of Cu and Zn disorder. This disorder in the cation sublattice is reported to reduce the band gap [61]. Due to the manifold possibility of the formation of defect complexes, CZTS is assumed to possess an electrically benign character.

## 5.5 Properties of Inks

Two different types of inks including micro and nano were synthesized without any capping agent. For comparison, pellets from micropowder were also synthesized. In this section, structural, optical and morphological properties of such inks and powder have been studied.

### 5.5.1 Structural, Morphological and Optical Properties of Micropowder

A typical X-ray diffractograph of powder is shown in Fig. 5.12. The X-ray diffraction (XRD) comprises sharp peaks at  $2\theta$  values of  $28.6^\circ$ ,  $47.3^\circ$ ,  $56.2^\circ$  and minute peak at  $76.4^\circ$ ; these peaks are found to match well with standard data for kesterite

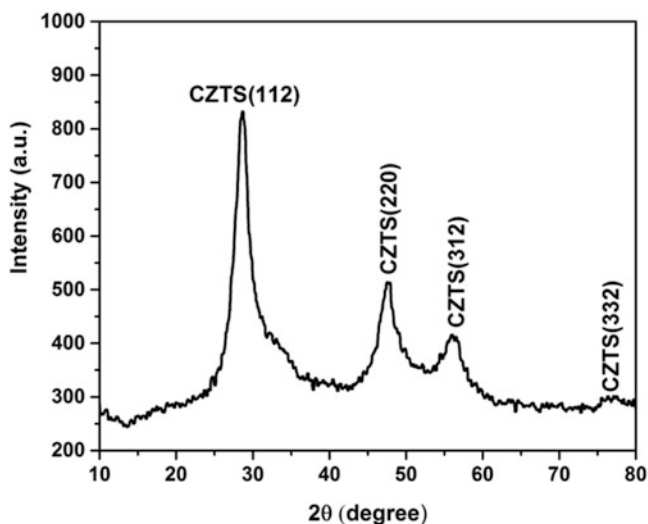
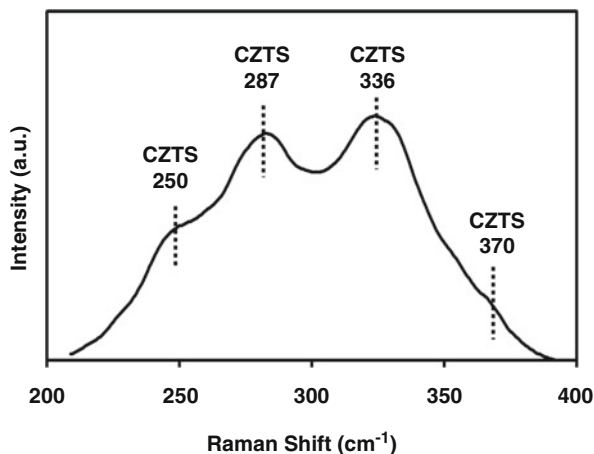


Fig. 5.12 X-ray pattern of CZTS powder heated at 473 K

**Fig. 5.13** Raman spectrum of CZTS powder



CZTS (JCPDS 26-0575) and are identified to be due to reflections from (112), (220), (312) and (332) planes, respectively. The sharpness of the (112) peaks suggests a good crystallinity. No other peaks such as  $\text{Cu}_x\text{S}$  or  $\text{SnS}_y$  were assigned which shows the powder is possibly CZTS.

The Raman spectrum of CZTS powder taken at room temperature is shown in Fig. 5.13. In general, the spectrum shows peaks at 250, 287, 336 and 370  $\text{cm}^{-1}$ . These peaks are characteristics of kesterite CZTS [49]. The main peak at 336  $\text{cm}^{-1}$  is due to the A1 vibrational mode, arising from the vibrations of the sulphur atoms in the CZTS lattice while the rest of the atoms remains stationary [50]. The peaks at 250 and 287  $\text{cm}^{-1}$  were allied to B symmetry mode while the peak at 370  $\text{cm}^{-1}$  has been assigned to B and E symmetry modes of CZTS [55]. Thus, it is confirmed that 473 K is sufficient for the formation of crystalline CZTS phase. Further, this vibrational feature is supported by theoretical calculations as well [62].

The surface morphology of the CZTS powder is observed using scanning electron microscopy (SEM) as shown in Fig. 5.14. The particles are agglomerate and form relatively large microparticles clusters. The powder is made of spherical particles of diameters about 0.6–0.8  $\mu\text{m}$ . Thus, the microwave-processed synthesis displays good homogeneity and compositional control.

The diffuse reflectance spectrum of CZTS microparticles (powder) is measured in the wavelength range of 300–2000 nm as shown in Fig. 5.15. The spectrum has a strong absorption below 900 nm due to absorption by the CZTS microparticles confirms its suitability of maximal solar photons absorption.

The optical band gap of CZTS powder has been estimated from diffuse reflectance spectrum using Kubelka–Munk function,  $F(R_\infty)$  [63]. Kubelka–Munk function can be expressed as:

$$F(R_\infty)h\nu = (h\nu - E_g)^{1/2} \quad (5.4)$$

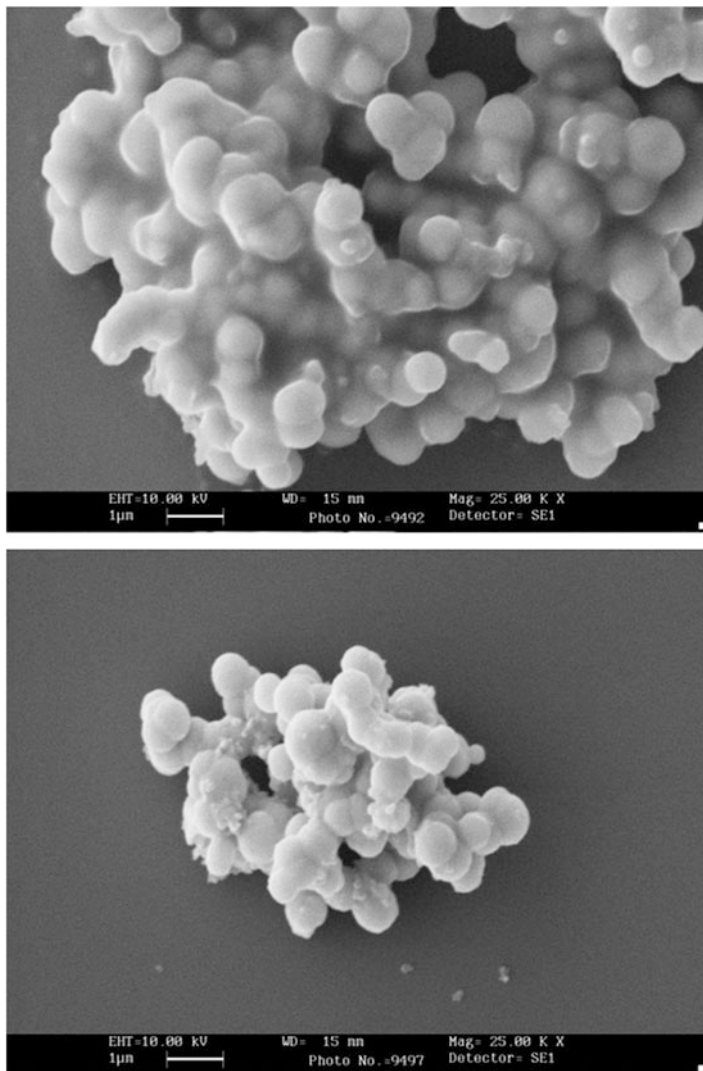


**Fig. 5.14** Scanning electron microscopy of CZTS powder

where  $F(R_\infty)$  is Kubelka–Munk function,  $h$  is Planck's constant,  $\vartheta$  wave number. The  $F(R_\infty)$  is obtained from diffuse reflectance

$$[F(R_\infty)] = \frac{(1 - R_\infty)^2}{(2R_\infty)} \quad (5.5)$$

$R_\infty = R(\%)/R_{\text{ref}}(\%)$ ,  $R_{\text{ref}}$ : diffuse reflectance of reference (in the present study, we use  $\text{BaSO}_4$  as a reference). Tauc plot of  $[F(R_\infty)h\nu]^2$  vs.  $h\nu$  is shown in Fig. 5.16. The band gap of CZTS powder as determined from the plot is found to be  $\sim 1.5$  eV.



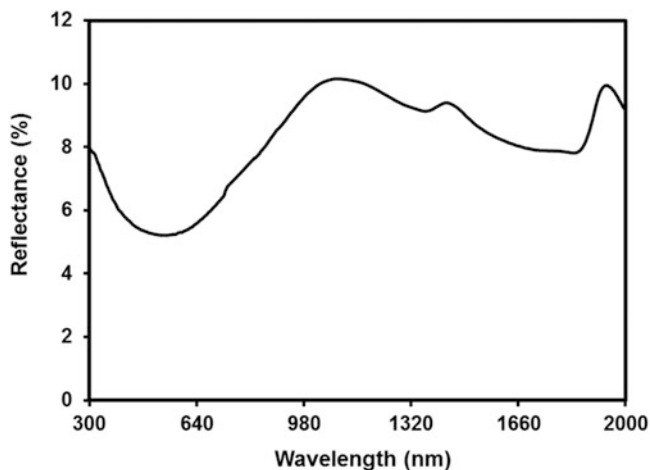


Fig. 5.15 Diffuse reflectance spectrum of CZTS powder

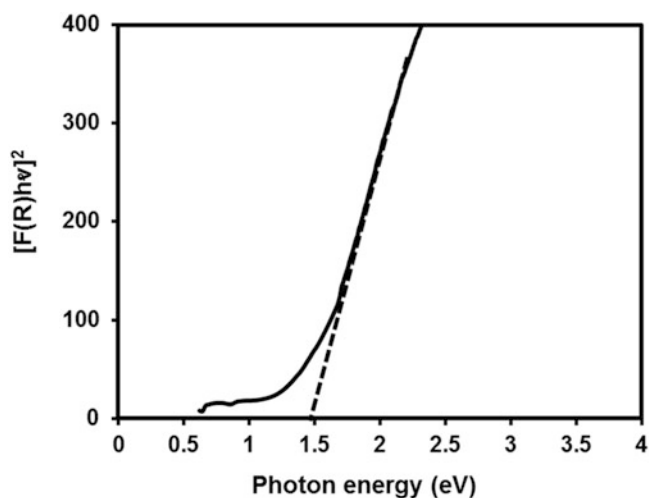
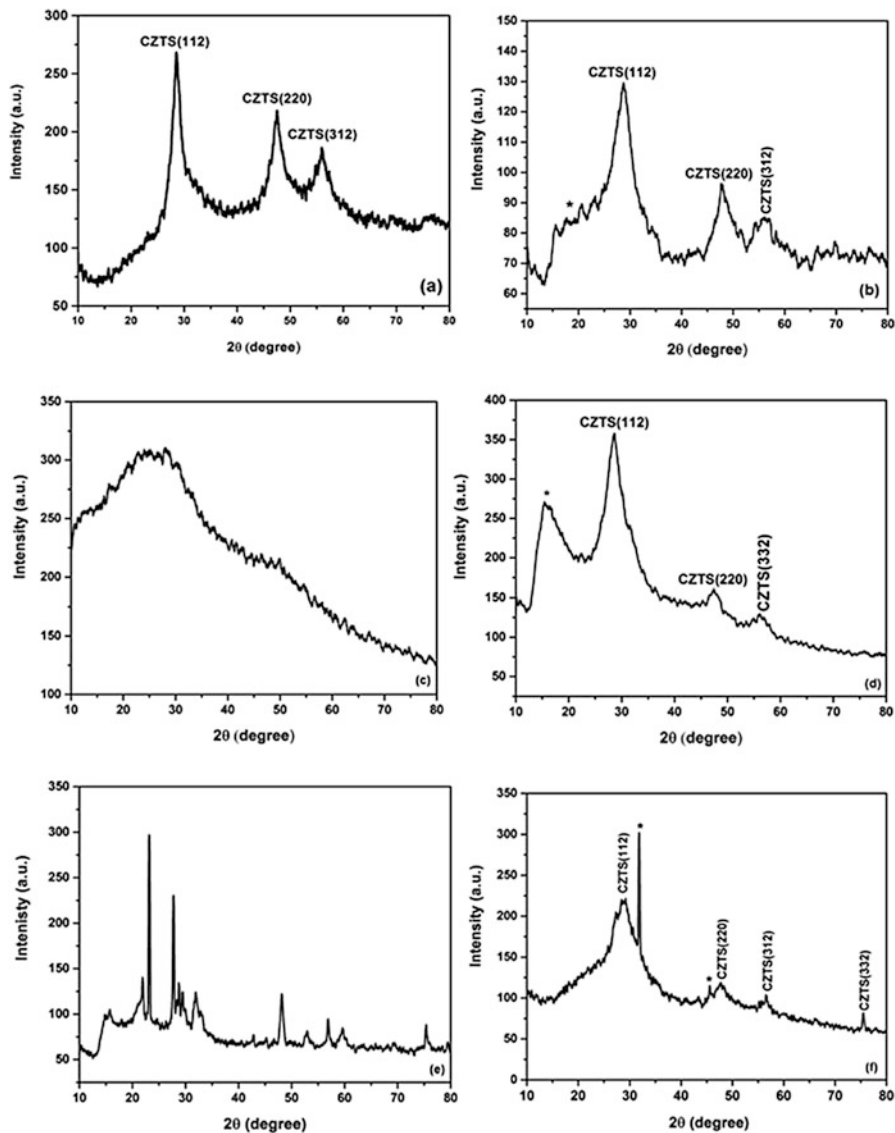


Fig. 5.16 Optical band gap using Kubelka–Munk function

### 5.5.2 Structural and Morphological Properties of Microparticles Ink

To analyse the crystalline structure and phase, X-ray diffraction of all the inks synthesized using different sulphur sources were performed. Figure 5.17 shows the XRD plots of inks drop cast into glass followed by vacuum dried at 373 K.



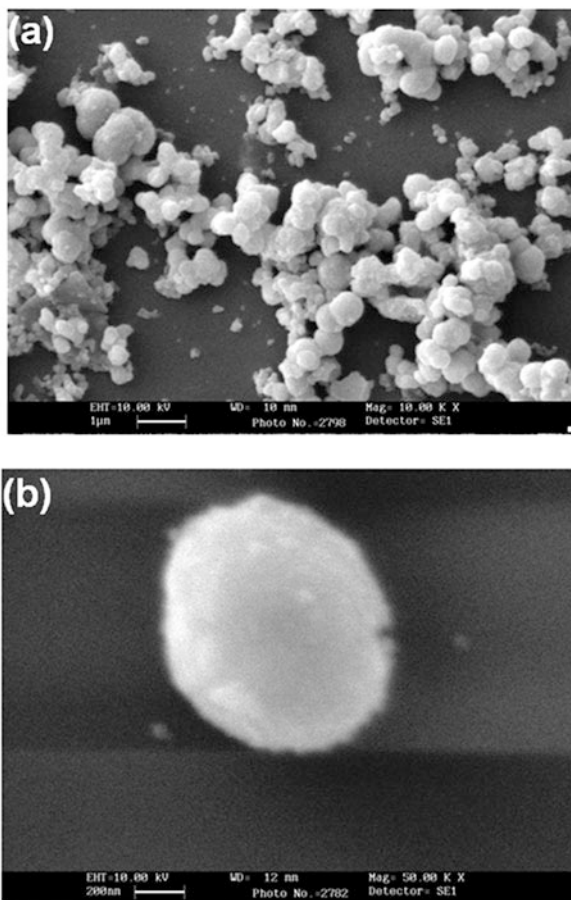
**Fig. 5.17** XRD plots of CZTS ink prepared using different sulphur sources: (a) thiourea, (b) thioacetamide, (c) sodium thiosulphate, (d) thioglycolic acid, (e) sulphur and (f) sodium sulphide

The XRD of all the samples (except for the sample prepared using thiourea) shows impurity (indicated as \*). Surprisingly, XRD of CZ (ST) shows no intense peak indicating amorphous nature of the particles (5.17 c) whereas those for CZ (SS) (5.17 e), peaks due to Na source along with CZTS phase has been found. The crystalline structure of the CZ (S) is unidentified. However, XRD plot of CZ

(TU) shows peaks due to tetragonal CZTS only and no other extra peaks are present inferring formation of pure CZTS. Three broad and intense peaks ascribed to the (112), (220) and (312) planes are detected (JCPDS-26-0575) for the CZTS ink prepared using TU. This result shows that microwave-processed CZTS ink in TU yields pure CZTS phase. Hence, further study is on CZTS-TU only (hereafter mentioned as CZTS).

Figure 5.18 shows the SEM images of the CZTS microparticles synthesized using TU as a sulphur source. Low and high magnification images reveal that prepared particles consist of large amount of sphere-like grains ranging from 0.8 to 1  $\mu\text{m}$ . Further CZTS microparticles are linked with adjacent ones to form chain-like network. The synthesis of sphere-like CZTS microparticles by microwave irradiation was also investigated by Kumar et al. [21].

**Fig. 5.18** (a) Low and (b) high magnification SEM images of CZTS microparticles



### 5.5.3 Characterizations of Nanoparticles Ink

The clarity of CZTS ink (Fig. 5.9) suggested that the CZTS particles are of nanoscale dimension. The shape and size of the NPs were determined by transmission electron microscopy (TEM). A typical TEM image of CZTS NPs is shown in Fig. 5.19. Nanoparticles are homogeneously distributed in the ink as revealed from the figure. The CZTS NPs are in general irregular with average diameters of 25–30 nm.

The transmittance spectrum of the CZTS NPs ink is measured in the wavelength range of 200–1200 nm as shown in Fig. 5.20. The spectrum reveals that ink has

**Fig. 5.19** Transmission electron microscopy of CZTS nanoparticles presented in ink [40]

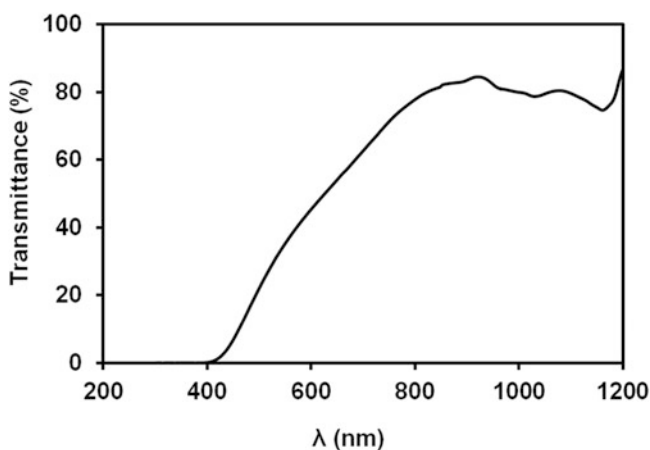
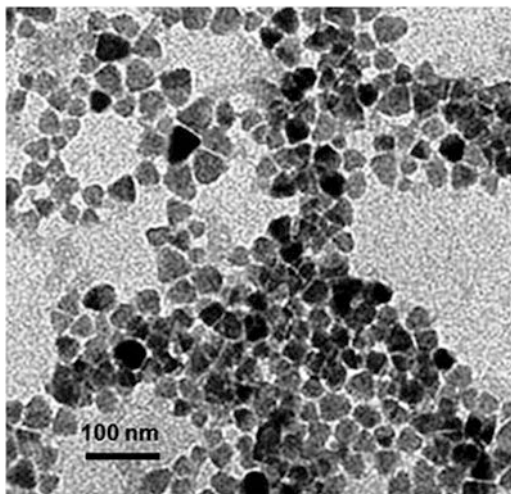
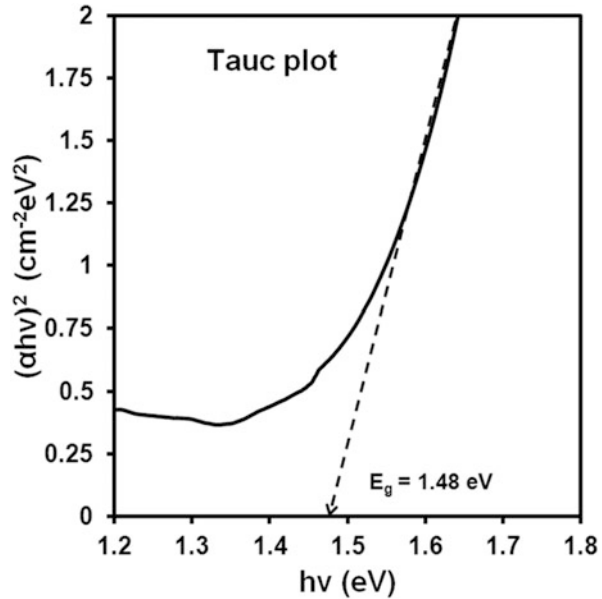


**Fig. 5.20** Transmittance spectrum of CZTS nanoparticle ink

**Fig. 5.21** Tauc plot of CZTS nanoparticle ink revealing band gap of 1.48 eV [40]



strong absorption below about 850 nm due to absorption by the CZTS particles showing its potential for solar cell application.

The band gap of the CZTS nanoparticles was estimated from the transmittance spectrum using Tauc plot for direct band gap semiconductors

$$\alpha h\nu = A(h\nu - E_g)^{1/2} \quad (5.6)$$

where

$\alpha$  is the absorption coefficient ( $\text{cm}^{-1}$ ),

$h$  is Plank's constant (J-s),

$\nu$  is the frequency of radiation (Hz),

$A$  is an appropriate constant and

$E_g$  is the band gap (eV).

The Tauc plot of  $h\nu$  versus  $(\alpha h\nu)^2$  is shown in Fig. 5.21. The band gap of the CZTS NPs determined by extrapolating the linear part of the plot is found to be 1.48 eV, which is in good agreement with 1.49 eV reported for the CZTS [2].

To check the reproducibility of inks, transmittance spectrum of two more samples have been measured in the wavelength range of 300–1500 nm (synthesized at different time duration) as shown in Fig. 5.22. However, the results were similar. Both the samples show absorption edge near 850 nm which is due to the CZTS nanoparticles.

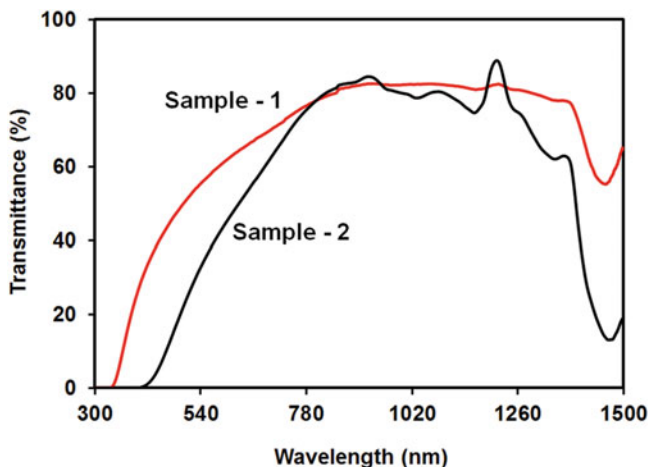


Fig. 5.22 Transmission spectrum of CZTS ink

## 5.6 Doctor Blade Coating of Films

The solution/inks were first deposited on prepared substrates. Surface preparation generally involves appropriate cleaning and drying in order to reduce the surface contamination and improve film adhesion and coating quality. The substrates used in this work for the deposition of the samples were 1.5 mm thick soda-lime glasses. The glass substrates were first cleaned in ultrasonic bath in mixture of water-chromic acid solutions followed by washed two times in bi-distilled water. The substrates were then cleaned with methanol two times. Finally, the substrates were dried in oven for 323–343 K for few minutes to avoid any contaminations.

Most of the groups working on kesterite use a two-step process in general, i.e. a low-temperature deposition combined with a high-temperature annealing step in S or Se [64]. The steps and critical parameters involved in ink printing of CZTS films are illustrated in Fig. 5.23. These methods work by coating a layer of precursor-containing solution on the surface of a substrate followed by appropriate thermal processing to yield the desired kesterite phase.

### 5.6.1 Doctor Blade Coating

Doctor blade is a simple, economical and direct-write printing technique which can deposit films on any type of substrate. It is amenable to large area deposition and suitable for roll-to-roll processing. It offers an advantage over conventional spin coating, dip coating and drop casting in terms of low materials consumption, surface roughness and control of films thickness. Doctor blading nowadays is

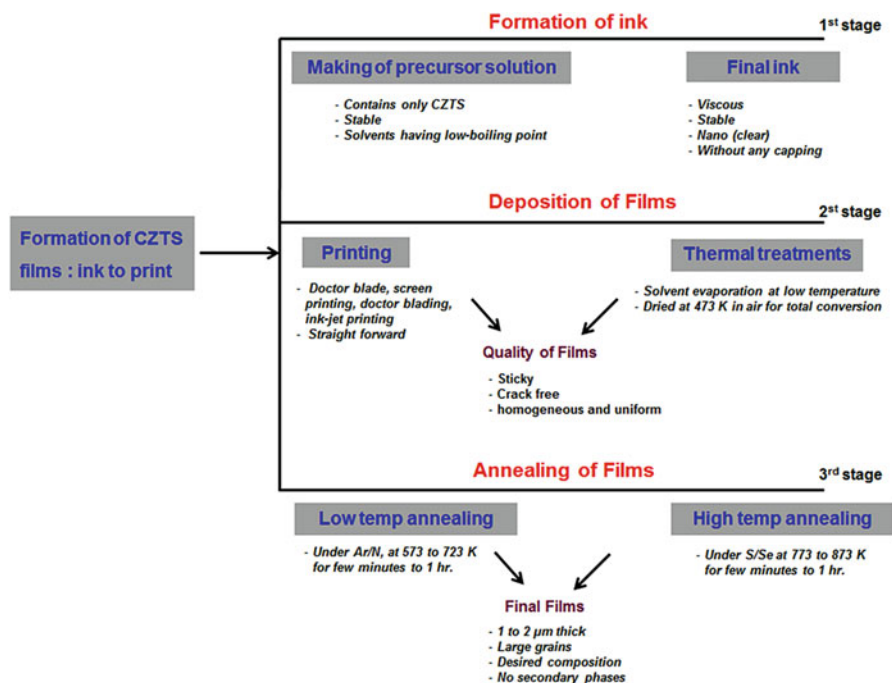


**Fig. 5.23** A general scheme for the coating of CZTS films: ink to print

widely used in fabrication of organic and dye-sensitized solar cells. Doctor blading-based processes are well-established techniques for the large-scale fabrication of ceramic substrates and related multilayered structures.

In principal, it uses a sharp blade at a fixed distance under which the coating liquid is deposited. The latter is then spread over the substrate by moving the blade at a constant rate. Figure 5.24 depicts the main stages involved in doctor blade technique. Compared to spin coating, doctor blading is relatively slow and it may happen that the dissolved material aggregates or crystallizes during processing. On the other hand, doctor blading is easily transferable and integrable into R-2-R fabrication concept, which is then often called knife-over-edge coating [64]. The Doctor Blade printer used in the present work is depicted in Fig. 5.25. It comprises two independent systems, i.e. blading part and applicator.

The finalized system was fabricated in our laboratory to combined blading and applicator. The blading part was provided by Royal Enterprises, Chennai, India. However, the applicator was delivered by Darteno Industries, Gujarat, India. For printing of films, the inks are directly deposited on glass substrate ( $75 \times 25 \text{ mm}^2$ ). The coating was done by sharp blade with a drawdown speed of 5 mm/s. The blade-to-substrate distance was 20  $\mu\text{m}$ . No temperature and/or vacuum were applied while depositing films. The technical specifications of the doctor blading are presented in Table 5.6.

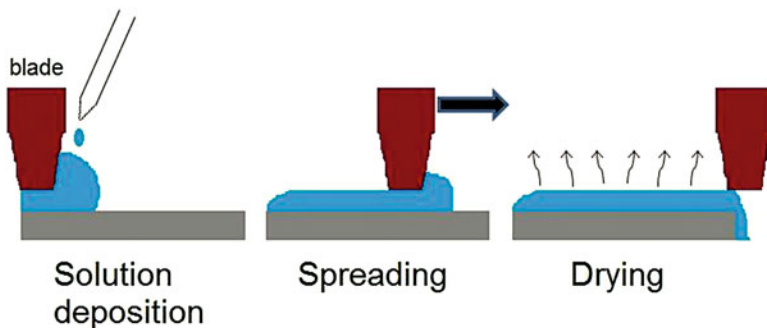


Fig. 5.24 Main stages involved in doctor blade technique [65]

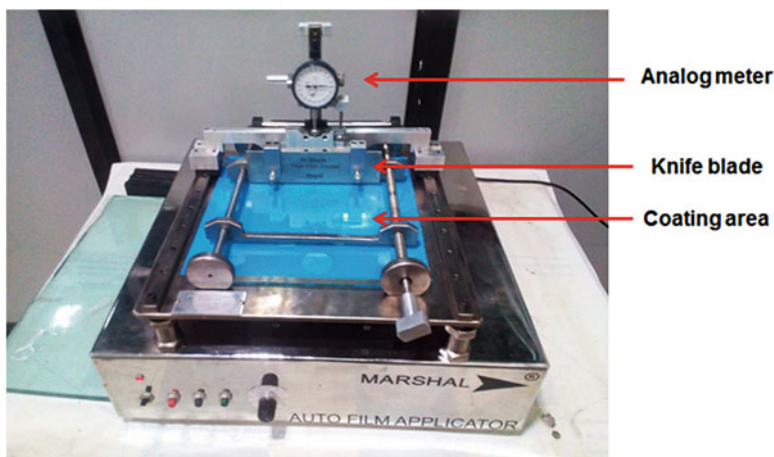


Fig. 5.25 Auto film applicator/Doctor Blading consisting of (1) Blading and (2) Applicator part

Table 5.6 Technical specifications of the thin film coater (Doctor Blade)

Mark and model	'Marshal' AP-E (basic)
Blade adjustable height	0–100 nm (from base to knife edge)
Coating area	200 × 200 mm
Wet film coating thickness	0–100 μm
Draw down speed	4.1–49 mm/s
Power supply	Single phase 220 V, 50 Hz
Weight	50 Kg
System	Automatic



## 5.7 CZTS Coating with Microwave-Processed Inks and Properties

Coating of CZTS films from different types of inks is one of the objective of this investigation. Two different types of inks were developed in preceding section. These inks are: (1) Microparticle ink (MPI) and (2) Nanoparticle ink (NPI). In this section, films deposited and characterized from these inks were studied.

### 5.7.1 Films Coated from Micro Ink

The XRD patterns of different heat-treated CZTS films are shown in Fig. 5.26. Diffractogram of the sample CZMP (Fig. 5.26a) shows broadlines at  $2\theta$  values of  $28.51^\circ$ ,  $47.31^\circ$  and  $56.11^\circ$ , which is identified to be due to reflections from (112), (220) and (312) planes of kesterite CZTS (Joint Committee on Powder Diffraction Standards, JCPDS 26-0575). No other XRD lines were found suggesting that pure CZTS has been synthesized. In case of CZMP350 sample (Fig. 5.26b), a hump at  $32.97^\circ$  along with all the diffraction peaks of sample CZMP is analysed. This peak is also found to be due to kesterite CZTS(200) (JCPDS 26-0575). However, two more peaks at  $26.9^\circ$  and  $51.2^\circ$  in addition to the standard kesterite CZTS lines were found in CZMP400 film. These additional peaks are probably because of the

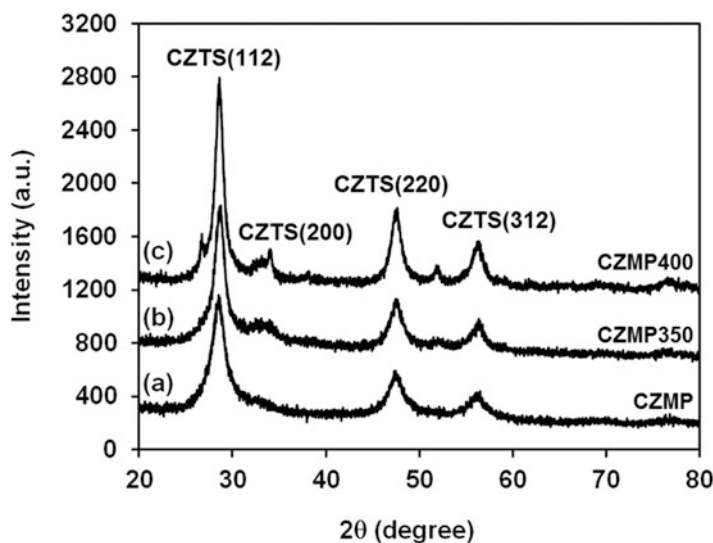


**Fig. 5.26** X-ray diffraction of CZTS films prepared from microparticle ink: (a) CZMP, (b) CZMP350 and (c) CZMP400 [66]

**Table 5.7** Average crystallite size of the CZTS films

Sample	Crystallite size (nm)
CZMP	5
CZMP350	7
CZMP400	10

presence of wurtzite CZTS (JCPDS 36-1450). Intensities of these peaks are very low with respect to the strongest peak of kesterite (112) at  $28.51^\circ$ .

In general, XRD lines of (112), (220) and (312) of CZMP400 films were more intense and sharper as compared to those of CZMP film (Fig. 5.26a). This result reveals that there is some enhancement in the crystallinity due to annealing effect. The average crystallite size of the CZTS film has been estimated according to full width at half maximum (FWHM) of diffraction peaks using Scherrer's formula,

$$\beta = \frac{k\lambda}{L\cos\theta} \quad (5.7)$$

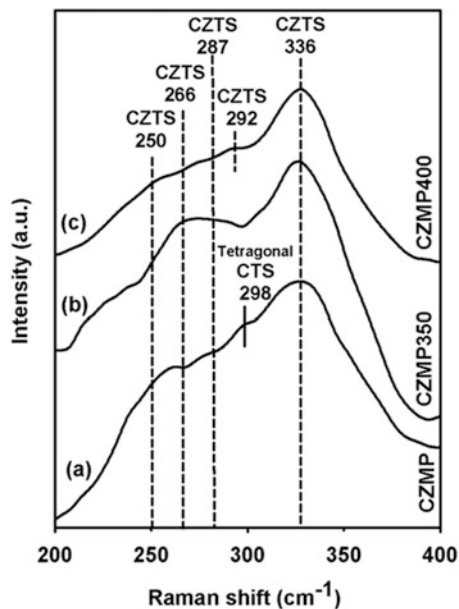
where  $\beta$  is the broadening of diffraction line measured at half maximum intensity (radians) and  $\lambda = 1.5418 \text{ \AA}$  is the wavelength of  $\text{CuK}\alpha$  X-ray radiation. The average crystallite size of the films obtained by measuring the broadening of most intense diffraction peak (112) is presented in Table 5.7. It is seen from Table 5.7 that crystallinity is considerably increased by increasing annealing temperatures. The temperature used in the preparation greatly affected the composition and crystallinity of the resulting samples.

Raman spectra of different types of CZTS films (CZMP, CZMP350 and CZMP400) are shown in Fig. 5.27. All the films, in general, show a strong peak at  $336 \text{ cm}^{-1}$  and accompanied by minute peaks at  $250$ ,  $266$  and  $287 \text{ cm}^{-1}$ . These peaks are due to kesterite CZTS and are in good agreement with previously reported Raman data [49, 66, 67] for CZTS.

The main peak at  $336 \text{ cm}^{-1}$  is due to the A1 vibrational mode, arising from the vibration of sulphur atoms in CZTS lattice while rest of the atoms remains stationary [49]. However, a small peak was found at  $298 \text{ cm}^{-1}$  in sample CZMP, which may be due to tetragonal CTS [68]. This peak is disappeared when annealed at  $632 \text{ K}$  (CZMP350) and  $673 \text{ K}$  (CZMP400) in Ar as shown in Fig. 5.27b, c. Further, intensity of the main peak increased slightly with increasing annealing temperatures which further shows crystallinity of the films improves with increasing annealing temperatures. This is consistent with results obtained from XRD. Hence, it is confirmed that CZTS films deposited from microwave-processed ink yield pure kesterite CZTS phase.

Scanning electron microscopy (SEM) is used to scrutinize the surface morphologies and cross sections of the CZTS films in order to define how the annealing temperature affected the surface morphology of the films. Figure 5.28 depicts the SEM top-view and cross-sectional images of three different types of CZTS films.

**Fig. 5.27** Raman spectra of CZTS films: (a) CZMP, (b) CZMP350 and (c) CZMP400 [66]



In general, the films are spongy comprising interconnected spherical grains. The film thickness is irregular since the films were deposited by a doctor blade technique using bar applicator with the thickness of 20  $\mu\text{m}$ . Further, the interface between the film and glass substrate is clearly distinct. From morphology of CZMP film (Fig. 5.28a), it is clearly seen that CZTS particles are agglomerated which can reduce the electrical transport properties of the films. The grains in CZMP film (Fig. 5.28b) are not fully formed and seem to be connected with ink which might be related with removing the TU and metal salts during heat treatments. Heat activates the loss of TU and metal salts which results in the formation of more holes in the precursor films. However, SEM images of the surface morphologies of the CZMP350 sample shows that the grains are well formed as smooth spheres. The CZTS films uniformly covered the substrates and the films are few microns thick, as shown in the cross-sectional SEM images (Fig. 5.28c). In case of sample CZMP400, the surface of the grains becomes rough and uneven. The spherical grains have diameters between 1.5 and 2  $\mu\text{m}$ . The cross-sectional SEM of the films shows that the surface of the CZMP350 film is smoother than that of CZMP or CZMP400. CZMP400 films have developed some overgrowths. It is clear from above discussion that the grain size increases with increasing annealing temperatures. This is also consistent with the results of XRD and Raman spectroscopy discussed above. In general, structurally and morphologically CZMP350 films showed better results.

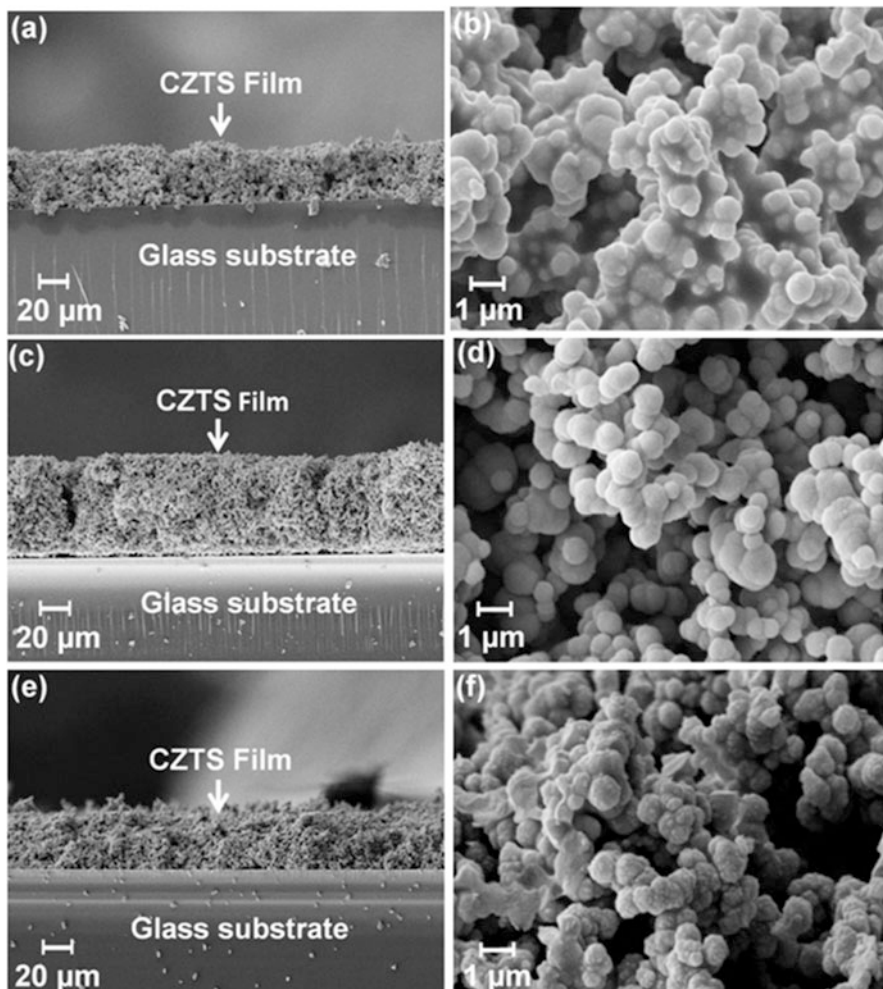
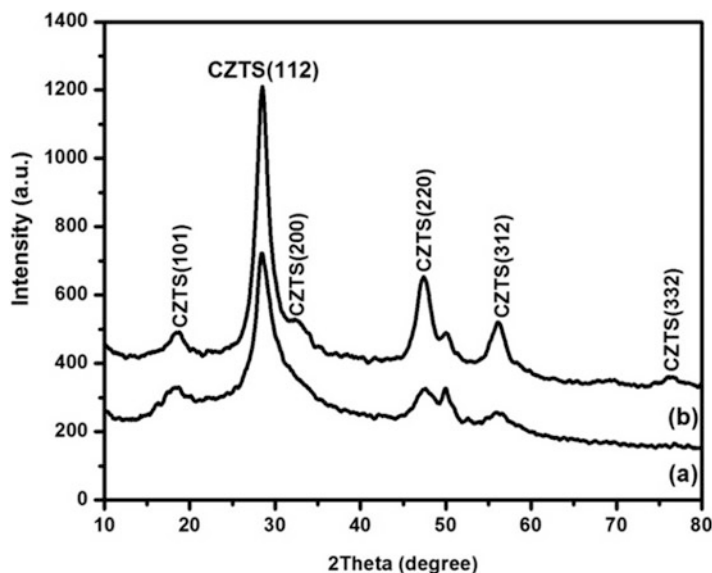


Fig. 5.28 SEM images of cross-sectional and top view of: (a, b) CZMP; (c, d) CZMP350; (e, f) CZMP400 films [66]

### 5.7.2 Films from Nano Ink

It was shown in the earlier section that the CZTS films coated from MPI yielded micro grains which in general were pores. The films coated by these inks were granular with average grain size of 1.5–2 μm. However, similar methods when employed with lower microwave power and lower concentrations, small grains with nanoparticles were achieved. The nanoparticle inks were used as it is for coating of films.



**Fig. 5.29** X-ray diffractograms of doctor bladed CZTS films on glass: (a) CZNP and (b) CZNP350 [40]

Figure 5.29 shows the XRD of CZNP and CZNP350 films. XRD plot reveals that printed CZTS films are polycrystalline. Diffraction peaks of both the films show the kesterite CZTS [JCPDS: 26-0575] with the peaks examined at  $2\theta$  values of  $18.29^\circ$ ,  $28.55^\circ$ ,  $47.58^\circ$  and  $56.39^\circ$  corresponding to the crystal planes of (101), (112), (220) and (312), respectively. However, upon annealing (Fig. 5.29b), two additional peaks at  $2\theta = 32.98^\circ$  and  $76.42^\circ$  have been observed. These peaks were also found to be due to kesterite CZTS(200) and CZTS(332) planes, respectively.

Table 5.8 compares the observed  $d$ -values of both the samples with standard JCPDS: 26-0575 data card. It can be seen from the table that all the XRD peaks of both the samples are matched exactly with JCPDS card revealing the formation of pure kesterite CZTS phase. The diffraction lines in annealed samples were sharper and stronger as compared to as-deposited which infers that annealing imparted improvement in crystallinity of the films. Further, a minute peak at  $49.93^\circ$  shrouded on CZTS (220) line ( $47.58^\circ$ ) was detected in as-deposited and annealed samples. To categorize this line, JCPDS files of probable compounds, such as  $\text{Cu}_3\text{SnS}_4$  (033-0501), tetragonal CTS (089-4714), ZnS (097-2204), SnS (039-0354),  $\text{SnS}_2$  (023-0677), CuS (06-0464) and  $\text{Cu}_2\text{S}$  (026-116), were examined.

However, it was found that none of them were exactly matched with this XRD line. The only (110) line of hexagonal  $\text{SnS}_2$  (JCPDS 023-0677) coincided with the unidentified line at  $49.93^\circ$ . But, the other intense XRD lines of  $\text{SnS}_2$ , such as (001) at  $15.029^\circ$ , (100) at  $28.2^\circ$  or (101) at  $32.125^\circ$ , were absent in the CZTS diffractograms as depicted in Fig. 5.29. Therefore, it is unclear whether this

**Table 5.8** Identification of observed XRD lines with standard CZTS (JCPDS)

Experimental		CZNP350		Standard JCPDS: 26-0575	
CZNP					
2 $\theta$ (degree)	<i>d</i> (nm)	2 $\theta$ (degree)	<i>d</i> (nm)	<i>d</i> (nm)	Indexing
18.29	0.48	18.29	0.48	0.48	CZTS(101)
28.55	0.31	28.55	0.31	0.31	CZTS(112)
–	–	32.98	0.27	0.27	CZTS(200)
47.58	0.19	47.58	0.19	0.19	CZTS(220)
56.39	0.16	56.39	0.16	0.16	CZTS(312)
–	–	76.42	0.12	0.12	CZTS(332)

particular XRD line is due to SnS<sub>2</sub> or not. The presence or absence of SnS<sub>2</sub> can be fixed by analysing Raman spectroscopy. Further, it has been found by earlier authors [22, 29] that microwave-processed CZTS nanoparticles also give rise to secondary phases. Hence, even though XRD studies of the present CZTS films did not reveal any unwanted phases, the conformational characterization technique would be Raman spectroscopy.

The Raman shift spectra along with deconvolution of peaks of two different types of CZTS films (CZNP and CZNP350) are shown in Fig. 5.30. Deconvolution of each spectrum was done using Gaussian and Lorentzian functions. The spectra, in general, show three peaks: a strong one at 332 cm<sup>-1</sup> and weaker ones at ~250 and 287 cm<sup>-1</sup>. These peaks are due to the kesterite CZTS and are in good agreement with formerly reported data for CZTS [49, 67]. The main peak at 332 cm<sup>-1</sup> is due to the A1 vibrational mode, arising from the vibrations of sulphur atoms in CZTS lattice while rest of the atoms remains stationary [50]. Here it should be noted that peak position of the A1 mode of CZTS varies from 338 to 330 cm<sup>-1</sup> according to the Raman excitation wavelength, synthesis process and film deposition parameters [49, 67]. The weaker peak at 252 cm<sup>-1</sup> is due to the B(TO LO)/E(TO LO) modes that can be detected only by polarization Raman measurements using selection rules [69].

For CZNP sample (Fig. 5.30a), the peaks are broad and the weaker peaks of 252 and 287 cm<sup>-1</sup> convolute the main strong peak of 332 cm<sup>-1</sup> to create a significant shoulder. However, after annealing (Fig. 5.30b), the peaks become sharper due to improvement in crystallinity. The main peak of 332 cm<sup>-1</sup> is significantly stronger than the other two peaks due to the enhancement of crystallinity. Raman peaks due to tetragonal CTS (297, 337 and 352 cm<sup>-1</sup>), cubic CTS (295-303 and 355 cm<sup>-1</sup>), orthorhombic CTS (318 cm<sup>-1</sup>), cubic ZnS (267, 303 and 356 cm<sup>-1</sup>), Cu<sub>2-x</sub>S (264 and 475 cm<sup>-1</sup>) and SnS<sub>2</sub> (215 and 315 cm<sup>-1</sup>) are absent revealing formation of kesterite CZTS. Hence, it is confirmed that CZTS films printed from microwave-processed nanoparticle ink yields pure kesterite CZTS phase.

The preceding section reveals that both the type of films was pure kesterite CZTS. Hence, optical properties of only as-deposited samples (CZNP) were measured. Transmittance spectra of number of as-deposited CZTS films were measured

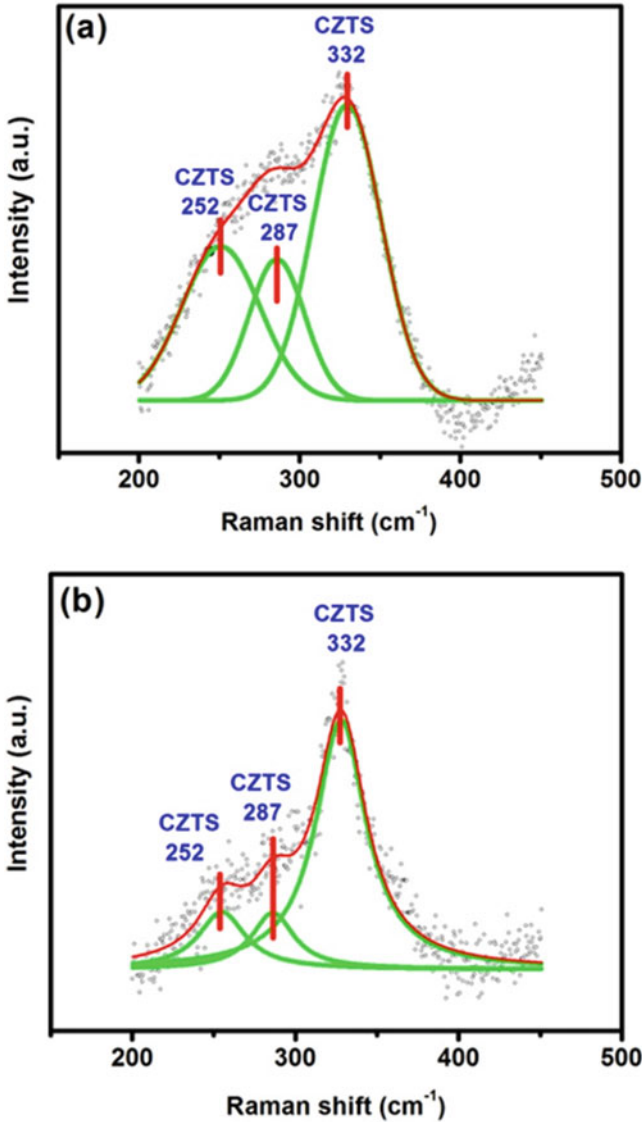


Fig. 5.30 Raman shift spectra of typical (a) CZNP and (b) CZNP350 films

in the wavelength range of 300–2400 nm as shown in Fig. 5.31. Almost all the samples show a similar trend. The spectra reveal that the films have strong absorption below about 850 nm due to absorption by the CZTS. The transmittance data is used to calculate the absorption coefficient ( $\alpha$ ) using following Eq. (5.8):

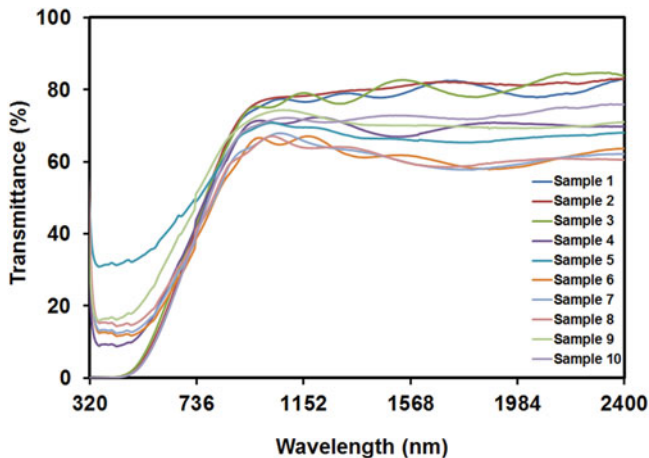


Fig. 5.31 Transmission spectra of as-deposited CZTS films

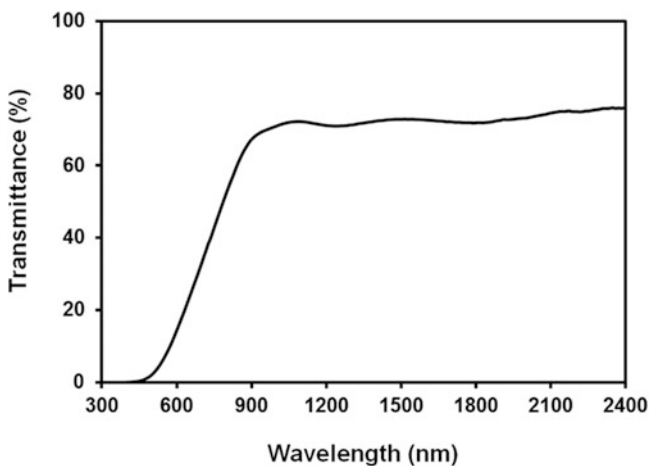


Fig. 5.32 Transmission spectrum of best CZTS films

$$\alpha = 1/d [\ln (1/T)] \quad (5.8)$$

where

$d$  is the thickness and

$T$  is the transmittance of the film.

The absorption coefficient of the CZTS films, in general, is determined to be  $>10^4 \text{ cm}^{-1}$  at the onset of the absorption edge. Transmittance spectrum of best CZTS films is shown in Fig. 5.32. Further, the transmittance data is also used to determine the band gap of the CZTS film using Tauc relation [70] for direct band gap semiconductors:



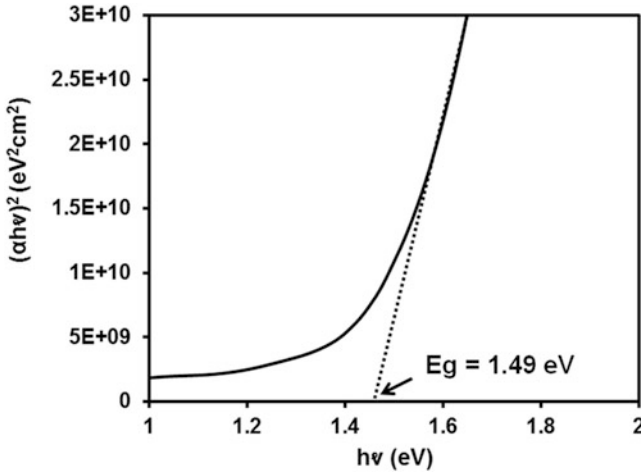


Fig. 5.33 Tauc plot of CZTS films showing band gap of 1.48 eV

$$\alpha h\nu = A(h\nu - E_g)^{1/2} \tag{5.9}$$

where

$\alpha$  is the absorption coefficient ( $\text{cm}^{-1}$ ),

$h$  is Plank’s constant (J-s),

$\nu$  is the frequency of radiation (Hz),

$A$  is an appropriate constant and

$E_g$  is the band gap (eV).

Figure 5.33 plots the band gap estimation from the curves of  $(\alpha h^2\nu)$  versus  $h\nu$ . Band gap values were given by extrapolating the straight line portion of the graph in the high absorption regime. The band gap of the films is found to be 1.49 eV which is in good agreement with earlier reported values of CZTS [2].

The microstructure of the CZTS films was studied by scanning electron microscopy. Figure 5.34 shows the typical cross-sectional view of both CZNP (Fig. 5.34a) and CZNP350 (Fig. 5.34b) films. The thickness of films is about 10  $\mu\text{m}$ . In general, the films consist of closely packed interconnected grains. This is completely different from micro grains as observed in the case of the films deposited from microparticle ink. In a word, microstructural properties are hugely affected by grain size. Nanoparticle reduces the diffusion between two particles joined together by boundaries in case of polycrystalline semiconductors which leads to increases in the packing fraction. The CZNP films contain irregular shaped grains of sizes from 0.2 to 0.4  $\mu\text{m}$  while CZNP350 films comprise spherical grains of sizes ranging from 0.6 to 0.8  $\mu\text{m}$ .

Further, the CZNP films had some voids between the grains which reduce on annealing as the film become smoother and compact. However, the CZNP350 films are still not as well-densified as those useful for solar cells [6].

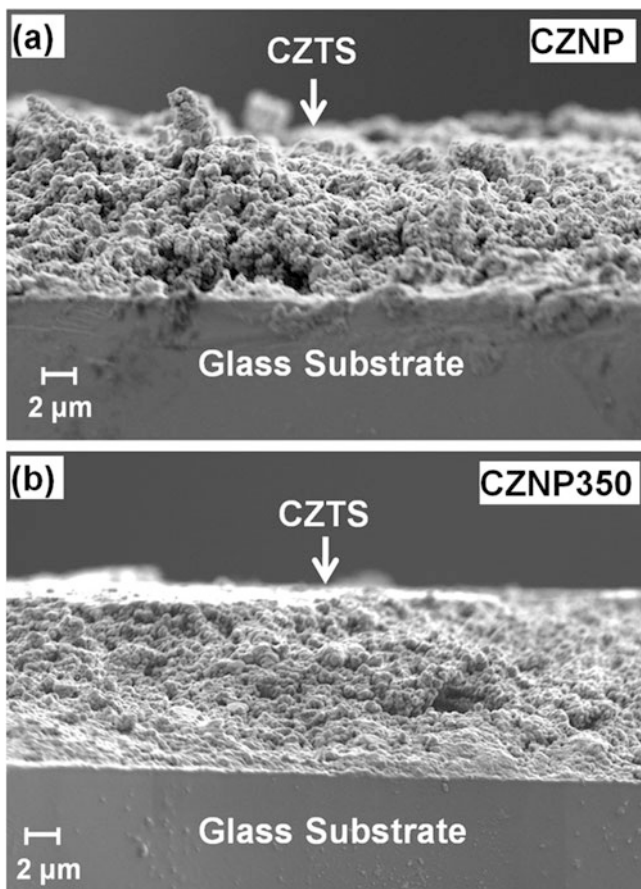


**Fig. 5.34** Scanning electron micrograph of the cross section of CZTS films: (a) CZNP and (b) CZNP350 [40]

The chemical composition of both the types of CZTS films examined from the Energy Dispersive X-ray Spectrum (EDS) revealed that the films to be CZTS exhibits the existence of only copper, zinc, tin and sulphur. The composition of the CZNP and CZNP350 films is Cu:Zn:Sn:S = 2.06:1.13:0.93:3.83 and 2.12:1.10:1.06:3.69, respectively, which is close to the theoretical value of 2:1:1:4. Both the samples were zinc-rich and tin poor.

Some interesting results from structural, optical and morphological properties may be summed up as follows:

- XRD and Raman spectroscopy confirms the formation of only kesterite CZTS phase.
- Band gap of the CZTS films was 1.49 eV.

- The grains are relatively compact and small compared to those obtained from microparticle ink.
- Grain size increases with increasing annealing temperatures.
- The thickness of the films is  $\sim 10 \mu\text{m}$  which is 4 times lower than that obtained from microparticle inks.
- Hence, the effect of microwave power and time on structural and morphological properties of CZTS films is clearly observed.

## 5.8 Electrical Properties

Preceding section described CZTS films deposited from two different types of inks, such as microparticle ink (MPI) and nanoparticle ink (NPI). This section reports the electrical properties from 77 to 500 K in dark and under illumination. Temperature variation of dark and conductivity under illumination of films from NPI was measured at different temperatures. Thermoelectric power (TEP) was also ascertained at room temperature ( $\sim 300$  K) to determine the carrier concentration. The films deposited from MPI were not suitable for electrical investigation since there were considerable voids between the grains (Sect. 5.7, Fig. 5.28). However, the microparticle pellets were examined in lieu of the MPI films [71].

### 5.8.1 Electrical Properties in Dark ( $\sim 300$ K)

Electrical conductivity ( $\sigma$ ) and thermoelectric power (TEP,  $\alpha_{\text{th}}$ ) of different types of CZTS films and micropowder pellets were measured in dark at room temperature ( $\sim 300$  K). The thermoelectric voltages generated by all the samples were positive indicating that they are  $p$ -type with holes as majority carriers.

Electrical conductivity ( $\sigma$ ) of a sample is given by the relation;

$$\sigma = p e \mu_p \quad (5.10)$$

where

$p$  is the hole concentration

$e$  is the charge of electron

$\mu_p$  is the mobility of holes

TEP ( $\alpha_{\text{th}}$ ) of a sample is given by

$$\alpha_{\text{th}} = k/e [A + \ln (N_v/p)] \quad (5.11)$$

where

$p$  is the concentration of holes ( $\text{cm}^{-3}$ ),

$N_v$  is the effective density of state in valance band ( $6.91 \times 10^{17} \text{ cm}^{-3}$  for CZTS),

$A$  is a scattering constant (4 for impurity scattering),

**Table 5.9** Electrical properties of different types of CZTS films in dark (~300 K)

Sample	TEP( $\mu\text{V/K}$ )	$\sigma$ (S/cm)	$n$ ( $\text{cm}^{-3}$ )	$\mu$ ( $\text{cm}^2 \text{V}^{-1} \text{s}^{-1}$ )
<i>Films from NPI</i>				
CZNP	+350	$3.5 \times 10^{-4}$	$1.3 \times 10^{18}$	0.003
CZNP350	+130	$4 \times 10^{-2}$	$1.2 \times 10^{19}$	0.35
<i>Films from MPI</i>				
CZMP	+640	0.007	$3.32 \times 10^{16}$	0.14
CZMP350	+326	0.086	$1.18 \times 10^{18}$	0.001
CZMP400	+130	0.22	$1.25 \times 10^{19}$	0.004

$k$  is the Boltzmann constant ( $86.7 \mu\text{V/K}$ ) and  $e$  is the electronic charge.

For each sample, Eq. (5.11) was used to derive  $p$  from the measured value of TEP. Further, Eq. (5.10) was then utilized to calculate  $\mu_p$  from measured value of  $\sigma$  and  $p$ . The electrical properties of different types of CZTS films and pellets are presented in Table 5.9.

Table 5.9 reveals that,

- Both types of films and pellets show  $p$ -type conduction with holes as majority carriers.
- The concentration of holes in as-deposited films is  $\sim 10^{18} \text{ cm}^{-3}$ ; however, it increases to  $\sim 10^{19} \text{ cm}^{-3}$  upon annealing (in case of NPI).
- In general, electrical conductivity and mobility of samples increases with increasing annealing temperatures.
- Mobility of as-deposited film increases to 10 times upon annealing.
- The films show photoconductivity.

### 5.8.2 Temperature Variation Electrical Conductivity of NPI Coated CZTS Films: 77–500 K

Temperature variation of electrical conductivity (TVEC) of a semiconductor sample elucidates how charge carriers move in the sample. The conductivities of CZTS films (NPI) have been measured in dark and under illumination at different temperatures varying from 77 to 500 K. The TVEC ( $\sigma$ ) of typical as-coated films was investigated in two parts: (1) Low temperatures region: 77–300 K and (2) High temperatures region: 300–500 K in dark and under different light intensities (100 and 190  $\text{mW/cm}^2$ ). Figure 5.35 shows the TVEC of CZTS films in dark ( $\sigma_D$ ) and under illumination ( $\sigma_L$ ) (intensity: 100 and 190  $\text{mW/cm}^2$ ) in the temperature range of 77–300 K. Figure 5.36 shows the TVEC of a typical CZTS film in the temperature range 300–500 K.

At lower temperature, the conductivity was found to be due to Mott-variable range hopping (M-VRH) which was not only confirmed by the starlight line of plot

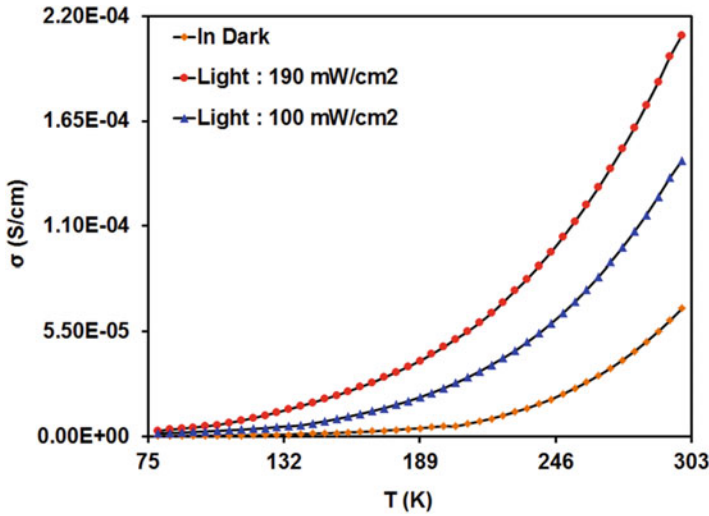


Fig. 5.35 Temperature variation of conductivity of typical CZNP film in dark and under light from 77 to 300 K

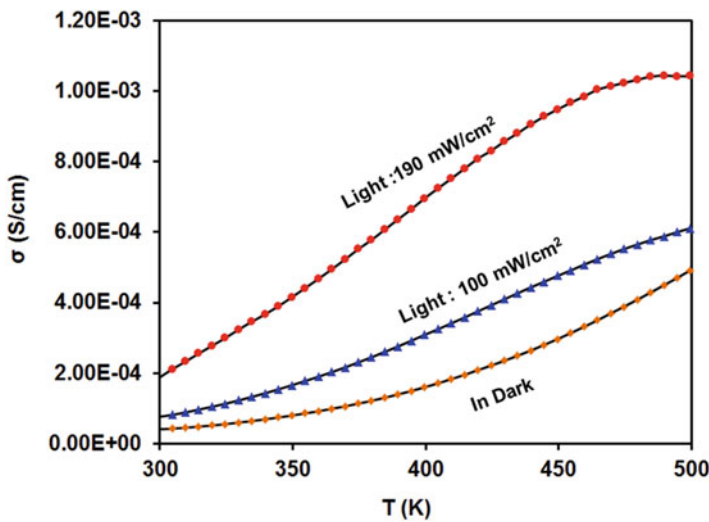
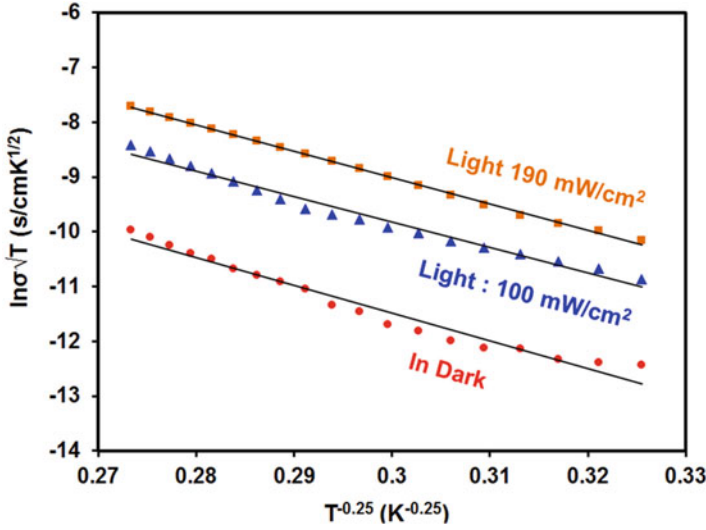


Fig. 5.36 Temperature variation of conductivity of typical CZNP film in dark and under light from 300 to 500 K

$\ln\sigma T^{0.5}$  vs.  $T^{-0.25}$  (Fig. 5.37) but also from the low hopping energy between 10 and 15 meV (Table 5.10) [39]. The basic mode of light remains unchanged even under different illumination intensities. However, hopping energy reduces linearly with increasing light intensities.



**Fig. 5.37** Plot of  $\ln\sigma\sqrt{T}$  vs.  $T^{-0.25}$  for CZNP films in dark and under light revealing M-VRH from 77 to 180 K

**Table 5.10** Hopping parameters of CZNP films in dark and under illumination

Light conditions	$\sigma_{oM}$ (S/cmK <sup>1/2</sup> )	$T_M \times 10^5$ (K)	$N_o(E_F) \times 10^{25}$ (cm <sup>-3</sup> eV <sup>-1</sup> )	$\bar{R}_{hop, Mott} \times 10^{-8}$ (cm)	$\bar{W}_{hop, Mott}$ (meV)
Dark	41.67	5	1.5	1	15
100 mW/cm <sup>2</sup>	64	4.6	1.6	0.9	14
190 mW/cm <sup>2</sup>	228	4.8	1.62	0.95	15

At intermediate temperatures (>50 to <300 K) Thermally Activated Conduction (TAC) is very possible, which can play crucial role in the conduction process of semiconductor thin films, as has been reported for polycrystalline CZTS films [72, 73]. For the TAC conduction mechanism, the temperature variation of dark conductivity can be written as:

$$\sigma = \sigma_0 \exp\left(-\frac{E_A}{k_b T}\right) \tag{5.12}$$

where

$\sigma_0$  is a constant,

$E_A$  is the activation energy in dark and

$k_b$  is the Boltzmann constant

The linear plot of  $\ln\sigma$  Vs.  $T^{-1}$  in dark and under light confirms TAC in the range of 200–300 K (Fig. 5.38). The activation energy is high compared to M-VRH and it decreases under light. The activation energies are indication of defects [40].

The CZTS films are polycrystalline and shows interconnected grains. Hence, it is expected that Grain Boundary Barriers (GBBs) will be formed at the interfaces of

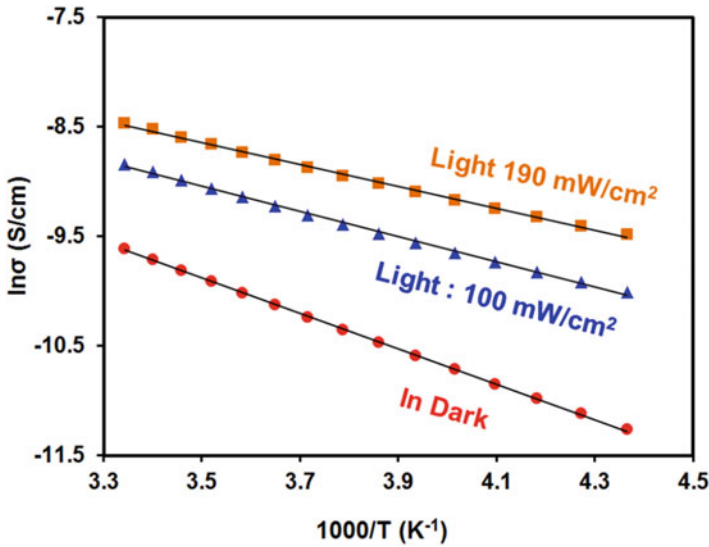


**Fig. 5.38** Electrical conduction due to activated band conduction of CZNP films in dark and under illumination from 200 to 300 K

the GBs [71, 72, 73]. The mode of transport will be found due to thermionic emission (TE) over GBBs [73]. Following Seto, the expression for the dark conductivity ( $\sigma_D$ ) of the CZTS films can be written as:

$$\sigma = \frac{\sigma_0}{T^{1/2} \exp\left(-\frac{E_B}{k_b T}\right)} \tag{5.13}$$

where

$\sigma_0$  is an appropriate constant

$T$  is the temperature

$E_B$  is grain boundary barrier height in dark

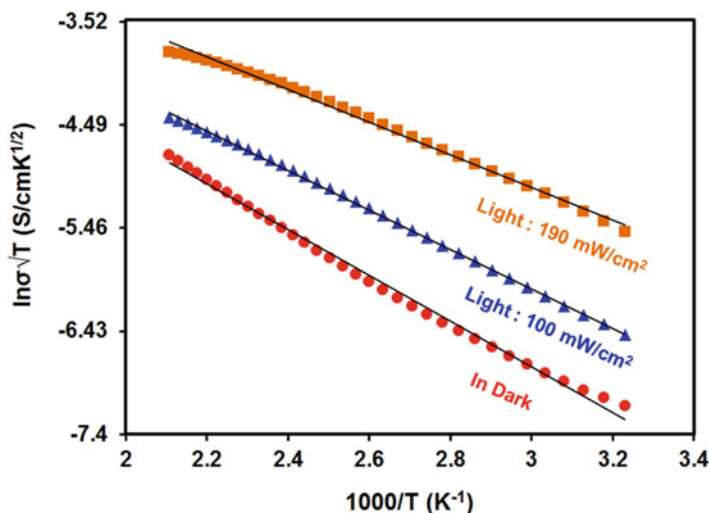
Hence, in the temperature region of 300–500 K, dominant mode of transport of holes is because of thermal emission over grain boundaries (Seto) and the activation energies denotes grain boundary barrier heights which is 180 meV in dark. The barrier height decreases due to illumination (Table 5.11). The straight line of  $\ln \sigma T^{1/2}$  vs.  $1000/T$  as shown in Fig. 5.39 confirms the validation of Seto’s model in CZTS films.

In general, the transport of holes in dark in these films is sum of M-VRH, TAC and TE over GB as:

$$\sigma_D = \sigma_{01MD} \exp\left(\left(-\frac{T_{MD}}{T}\right)^{1/4}\right) + \sigma_{02D} \exp\left(-\frac{E_{TACD}}{k_b T}\right) + \frac{\sigma_{03D}}{T^{1/2} \exp\left(-\frac{E_{BD}}{k_b T}\right)} \tag{5.14}$$

**Table 5.11** Activation energy of CZNP films in dark and under light

Temperature range (K)	Activation energy (meV)		
	In dark	Light: 100 mW/cm <sup>2</sup>	Light: 190 mW/cm <sup>2</sup>
200–300: TAC	140	99	86
300–500: TE over GB	180	160	130

**Fig. 5.39** Plot of  $\ln\sigma\sqrt{T}$  vs.  $1000/T$  for CZNP films in dark and under different light intensities: 300–500 K

However, under illumination the above equation is modified as:

$$\sigma_L = \sigma_{01ML} \exp\left(\left(-\frac{T_{ML}}{T}\right)^{\frac{1}{3}}\right) + \sigma_{02L} \exp\left(-\frac{E_{TACL}}{k_b T}\right) + \frac{\sigma_{03L}}{T^{\frac{1}{3}} \exp\left(-\frac{E_{BL}}{k_b T}\right)} \quad (5.15)$$

## 5.9 Solar Cells with CZTS Coatings

Apart from the physical properties of the absorber layer, understanding of solar cell structure is also required to further increase the device efficiency. One benefit of studying CZTS is that much of the knowledge regarding CIGS can be directly extended to kesterite CZTS simply by replacing CIGS absorber layer with *p*-type CZTS thin films.



### 5.9.1 Basic Structure

A typical structure (substrate) of solar cells based on kesterite CZTS absorber is depicted in Fig. 5.40. In general, the structure consists of 4–5 layer stacked on each other. Generally, CZTS solar cells are grown in a 'substrate' configuration (Fig. 5.40).

Highest efficiencies of 12.7% and 8.9% have been reported for CZTSSe and CZTS solar cells, respectively, on glass by IBM. Glass is a most commonly used substrate; however, efforts have been made to develop flexible solar cells on polyimide and metal foils. It consists of a substrate that acts as a support for the electrode layer, which is a few hundred nm thick molybdenum (Mo) films, usually deposited on the glass by sputtering. Mo is generally used as a back contact. On top of back contact, the *p*-type CZTS absorber layer with thickness ranging from 1 to 2.0  $\mu\text{m}$  is deposited. A variety of vacuum and non-vacuum techniques have been employed for the deposition of *p*-type absorber layer. At the interface, a thin 50–70 nm layer of CdS (*n*-type), typically referred to as buffer layer, has been deposited on absorber layer by conventional chemical bath deposition technique, thus forming *p-n* junction, which allows charge separation. The finalization of the cell proceeds then with the sputtering of a bilayer of ZnO-based transparent conducting oxides (TCOs): intrinsic zinc oxide (*i*-ZnO) and aluminium doped ZnO (AZO) are the most common. The solar cell is then completed with a metal contact grid and an  $\text{MgF}_2$  anti-reflection coating, used to enhance the charge collection and to reduce the reflected light loss, respectively.

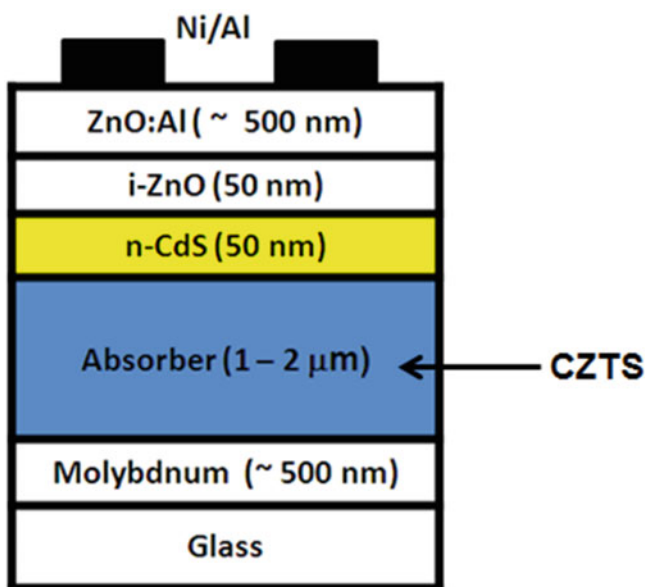


Fig. 5.40 Typical substrate structure of CZTS solar cell

### 5.9.2 Device Efficiency

CZTS/CZTSe/CZTSSe solar cells have been fabricated by vacuum and non-vacuum solution-based processes. The highest efficiency of 12.7% has been obtained for CZTSSe solar cells fabricated from ink-based deposition technique. Table 5.12 presents the properties of CZTS solar cells produced by different techniques.

**Table 5.12** Photovoltaic properties of CZTS/Se/SSe solar cells

Group/authors	Absorber deposition method	V <sub>OC</sub> (mV)	J <sub>SC</sub> (mA/cm <sup>2</sup> )	Fill factor (%)	Efficiency (%)
HZB (2015) Lin et al. [74]	Solution: Inkjet printing	428	31.3	65.9	8.8
<b>IBM (2014) Kim et al. [7]<sup>a</sup></b>	<b>Ink (Slurry): Spin coating</b>	<b>466</b>	<b>38.9</b>	<b>69.8</b>	<b>12.7</b>
CHARUSAT (2014) Tiwari et al. [72]	Solution based: Ion-exchange	521	19.13	62	6.17
Osaka Univ. (2014) Jiang et al. [75]	Electrodeposition: Cu/Zn/Sn stack	719	17.7	62.9	8
SUNY-Binghamton (2014) Dhakal et al. [76]	Vacuum: Co sputtering sulphurization	603	19	55	6.2
UNSW (2014) Su et al. [77]	Solution: Sol-gel	610	14.82	58	5.1
Dupont (2014) Wu et al. [78]	Solution: Spin coating	428	31.3	65.9	8.8
Washington Univ. (2014) Xin et al. [79]	Solution: Spin coating	443	31.2	60.2	8.32
IMRA Europe (2014) Larramona et al. [80]	Solution: water- ethanol spray coating	460	30.9	60	8.6
Purdue (2014) Miskin et al. [81]	Solution: Doctor blade	404	35.1	63.7	9
IMEC, Solliance (2013) [82]	Vacuum: sputtering/ selenization	410	38.9	61	9.7
ZSW (2013) Schnabel et al. [5]	Solution: Doctor blade	–	–	–	10.3
<b>IBM (2012) Shin et al. [83]<sup>a</sup></b>	<b>Vacuum: co-evaporation</b>	<b>661</b>	<b>19.5</b>	<b>65.8</b>	<b>8.9</b>
NREL (2012) Repins et al. [84]	Vacuum: co-evaporation	377	37.4	64.9	9.15
UCLA (2012) Yang et al. [85]	Solution: Spin coating	409	32.25	61	8.1

<sup>a</sup>Highest efficient solar cells based on selenides and pure sulphide CZTS absorber layer, respectively in Reference [7] and [83]

Table 5.12 reveals that:

- Efficient CZTS TFSCs can be fabricated by diverse deposition techniques, such as co-evaporation, sputtering, electrodeposition, ion-exchange and direct ink coating techniques.
- The highest efficiency of 12.7% has been achieved by IBM (USA) for CZTSSe TFSC direct deposited from ink/slurry of non-CZTS particles in toxic hydrazine.
- For vacuum-deposited TFSCs, the highest efficiency attained is 9.7% for CZTSe by IMEC/Solliance (Europe).
- In India, our group (Tiwari et al. [72]) has made 6.17% efficient CZTS TFSCs by a unique ion-exchange solution technique. This is a record for all solution-processed CZTS solar cells.
- CZTS films deposited by simple, non-vacuum, direct-write and solution-based techniques, like spin coating and doctor blading, have yielded the TFSCs with relatively higher efficiencies of 8–12.7%.

## 5.10 Concluding Remarks and Future Prospects

The microwave process is a simple and solution-based method for obtaining solar quality kesterite CZTS absorbers. High-quality CZTS nanoparticles have been achieved using such technique without using either capping or tedious sulphurization process. CZTS ink is found to be suitable for coating the films. Films with different structures, including micro and nano grains, have been coated from inks. CZTS films coated from nanoparticle ink seems to be promising and shows better electronics properties compared to those of microparticle ink. Since the ink is found to be suitable for solar cells, it is now desirable to fabricate CZTS/CZTSSe solar cells from such ink in substrate and superstrate structure. Optimization of each layer with respect to the structure, composition and processing must be done to compare the results with other conventional and well-studied semiconductor such as CIGS and CdTe.

Further, it has been observed in the literature that the extra addition of Na plays a significant role in improving the structural, morphological and electrical properties of the resulting absorber layers (CIGS, CIS and CZTS). Hence, CZTS solar cells should also be fabricated by incorporating appropriate Na either in precursor solution or in finalized films.

**Acknowledgments** The authors are grateful to the President and Provost of Charotar University of Science and Technology, Changa, Anand, Gujarat, India, for providing research facilities. Helpful discussion from Dr. Maykel Courel, National Autonomous University of Mexico (UNAM), Mexico, is highly appreciated.

## References

1. H. Azimi, Y. Hou, C.J. Brabec, *Energy Environ. Sci.* **7**, 1829 (2014)
2. K. Ito, *Copper zinc tin sulfide-based thin-film solar cells* (Wiley, Chichester, 2015)
3. R.H. Bube, *Photovoltaic materials, series on properties of semiconductor materials*, vol 1 (Imperial College Press, London, 1998)
4. S. Ji, C. Ye, *Rev. Adv. Sci. Eng.* **1**, 42 (2012)
5. [http://www.semiconductor-today.com/news\\_items/2013/NOV/ZSW\\_261113.shtml](http://www.semiconductor-today.com/news_items/2013/NOV/ZSW_261113.shtml)
6. W. Wang, M.T. Winkler, O. Gunawan, T. Gokmen, T.K. Todorov, Y. Zhu, D.B. Mitzi *Adv. Energy Mater.* **4**, 1301465 (2014)
7. J. Kim, H. Hiroi, T.K. Todorov, O. Gunawan, M. Kuwahara, T. Gokmen, D. Nair, M. Hopstaken, B. Shin, Y.S. Lee, W. Wang, H. Sugimoto, D.B. Mitzi *Adv. Mater* **26**, 7427 (2014)
8. B. Flynn, W. Wang, C.-H. Chang, G.S. Herman, *Phys. Status Solidi (a)* **209**, 2186 (2012)
9. S. Riha, B. Parkinson, A. Prieto, *J. Am. Chem. Soc.* **131**, 12054 (2009)
10. Q. Guo, H. Hillhouse, R. Agrawal, *J. Am. Chem. Soc.* **131**, 11672 (2009)
11. Y. Liu, J. Xu, Z. Ni, G. Fang, W. Tao, *J. Alloys Compd.* **630**, 23 (2015)
12. M. Cao, Y. Shen, *J. Cryst. Growth* **318**, 1117 (2011)
13. R. AdhiWibowo, E. Soo Lee, B. Munir, K.H. Kim, *Phys. Status Solidi (a)* **204**, 3373 (2007)
14. N. Mirbagheri, S. Engberg, A. Crovetto, S.B. Simonsen, O. Hansen, Y.M. Lam, J. Schou, *Nanotechnology* **27**, 185603 (2016)
15. S. Engberg, Z. Li, J. Yan Lek, Y. Ming Lamb, J. Schou, *RSC Adv.* **5**, 96593 (2015)
16. C. Steinhagen, M.G. Panthani, V. Akhavan, B. Goodfellow, B. Koo, B.A. Korgel, *J. Am. Chem. Soc.* **131**, 12554 (2009)
17. T. Kameyama, T. Osaki, K.-I. Okazaki, T. Sb, A. Kudo, S. de Kuwabata, T. Torimoto, *J. Mater. Chem.* **20**, 5319 (2010)
18. Y.-L. Zhou, W.-H. Zhou, Y.-F. Du, M. Li, S.-X. Wu, *Mater. Lett.* **65**, 1535 (2011)
19. O. Zaberca, F. Oftinger, J.Y. Chane-Ching, L. Datas, A. Lafond, P. Puech, A. Balocchi, D. Lagarde, X. Marie, *Nanotechnology* **23**, 18540 (2012)
20. X. Yang, J. Xu, L. Xi, Y. Yao, Q. Yang, C.Y. Chung, C. Lee, *J. Nanopart. Res.* **14**, 931 (2012)
21. R. Kumar, B. Ryu, S. Chandramohan, J. Seol, S. Lee, *C. Hong Mater. Lett.* **86**, 174 (2012)
22. S. Shin, J. Han, C. Park, A. Moholkar, J. Lee, J. Kim, *J. Alloys, Compd.* **516**, 96 (2012)
23. W. Wang, H. Shen, X. He, *Mater. Res. Bull.* **48**, 3140 (2013)
24. P. Sarswat, M. Free, *J. Cryst. Growth* **372**, 87 (2013)
25. G. Wang, P. Chen, C. Tseng, *Cryst. Eng. Comm* **15**, 9863 (2013)
26. T. Knustson, P. Hanson, E. Aydil, *R. Penn. Chem. Commun.* **50**, 5902 (2014)
27. Y. Zhao, W. Tao, J. Liu, A. Wei, *Mater Lett* **148**, 63 (2015)
28. W. Wang, H. Shen, H. Yao, J. Li, J. Jiao, *J. Mater. Sci. Mater. Electron* **26**, 1449 (2015)
29. Y.-H. Lin, S. Das, C.-Y. Yang, J.-C. Sung, C.-H. Lu, *J. Alloys Compd.* **632**, 354 (2015)
30. T. Martini, C. Chubilleau, O. Poncelet, A. Ricaud, A. Blayo, C. Martin, K. Tarasova, *Sol. Energy Mater. Sol. Cells* **144**, 657 (2016)
31. H.W. Hillhouse, M.C. Beard, *Curr Opin, Colloid Interface Sci* **14**, 245–249 (2009)
32. R. Kumar, B. Ryu, S. Chandramohan, J. Seol, S. Lee, C. Hong, *Mater. Lett.* **86**, 174 (2012)
33. S. Shin, J. Han, C. Park, A. Moholkar, J. Lee, J. Kim, *J. Alloys Compd.* **516**, 96 (2012)
34. C.O. Kappe *Angew, Chem. Int. Ed* **43**, 6250 (2004)
35. B.J. Hayes, *Microwave synthesis: chemistry at the speed of light* (CEM Publications, Matthews, NC, 2002)
36. T.K. Chaudhuri, D. Tiwari, *Sol. Energy Mater. Sol. Cells* **101**, 46 (2012)
37. Jardine, F. H. in Emeleus, H. J. and Sharpe, A. G. (Ed.), *Advances in Inorganic chemistry and Radiochemistry*, 17 (1975) 133, Academic Press, USA
38. P.R. Ghediya, T.K. Chaudhuri, D. Vankhade, *J. Alloys Compd.* **685**, 498 (2015)
39. P.R. Ghediya, T.K. Chaudhuri, J.R. Ray, *AIP Conf. Proc.* **1728**, 020020 (2016)
40. P.R. Ghediya, T.K. Chaudhuri, *J. Phys. D. Appl. Phys.* **48**, 455109 (2015)

41. R. Wagner, H.D. Wiemhöfer, *J. Phys. Chem. Solids* **44**, 801 (1983)
42. C. Malerba,  $\text{Cu}_2\text{ZnSnS}_4$  thin films and solar cells: material and device characterization, an investigation into the stoichiometry effect on CZTS microstructure and optoelectronic properties, Ph.D. Thesis, University of Trento, Italy, 2014
43. T. Tanaka, T. Nagatomo, D. Kawasaki, M. Nishio, Q. Guo, A. Wakahara, A. Yoshida, H. Ogawa, *J. Phys. Chem. Solids* **66**, 1978 (2005)
44. K. Wang, B. Shin, K.B. Reuter, T. Todorov, D.B. Mitzi, S. Guha, *Appl. Phys. Lett.* **98**, 051912 (2011)
45. D.B. Mitzi, O. Gunawan, T.K. Todorov, K. Wang, S. Guha, *Sol. Energy Mater. Sol. Cells* **95**, 1421 (2011)
46. A. Walsh, S. Chen, S.-H. Wei, X.-G. Gong, *Adv. Energy Mater.* **2**, 400 (2012)
47. P.A. Fernandes, P.M.P. Salome, A.F. da Cunha, *Thin Solid Films* **517**, 2519 (2009)
48. X. Fontane, L. Calvo-Barrio, V. Izquierdo-Roca, E. Saucedo, A. Perez-Rodriguez, J.R. Morante, D.M. Berg, P.J. Dale, S. Siebentritt, *Appl. Phys. Lett.* **98**, 181905 (2011)
49. A.-J. Cheng, M. Manno, A. Khare, C. Leighton, S.A. Campbell, E.S. Aydil, *J. Vac. Sci. Technol. A* **29**, 051203 (2011)
50. M. Himmrich, H. Haeuseler, *Spectrochim. Acta A Mol. Biomol. Spectrosc.* **47**, 933 (1991)
51. M. Guc, S. Levcenko, V. Izquierdo-Roca, X. Fontane, L.V. Volkova, E. Arushanov, A. Pérez-Rodríguez, *Sci. Rep* **6**, 19414 (2016)
52. M.I. Khalil, O. Atici, A. Lucotti, S. Binetti, A. Le Donne, L. Magagnin, *Appl. Surf. Sci.* **379**, 91 (2016)
53. Y. Xi, Z. Chen, Z. Zhang, X. Fang, G. Liang *Nanoscale, Res. Lett.* **9**, 208 (2014)
54. B. Flynn, I. Braly, P.A. Glover, R.P. Oleksak, C. Durgan, G.S. Herman, *Mater. Lett.* **107**, 214 (2013)
55. G. Altamur, J. Vidal, *Chem. Mater.* **28**, 3540 (2016)
56. S.Y. Chen, A. Walsh, X.G. Gong, S.H. Wei, *Adv. Mater.* **25**, 1522 (2013)
57. S. Chen, J.H. Yang, X.G. Gong, A. Walsh, S.H. Wei, *Phys. Rev.* **B81**, 245204 (2010)
58. A. Nagoya, R. Asahi, R. Wahl, G. Kresse, *Phys. Rev. B* **81**, 113202 (2010)
59. S. Das, S.K. Chaudhuri, R.N. Bhattacharya, K.C. Mandal, *Appl. Phys. Lett.* **104**, 192106 (2014)
60. S. Chen, L. Wang, A. Walsh, X.G. Gong, S.H. Wei, *Appl. Phys. Lett.* **101**, 223901 (2012)
61. M. Kumar, A. Dubey, N. Adhikari, S. Venkatesan, Q. Qiao, *Energy Environ. Sci.* **8**, 3134 (2015)
62. Y. Gang Zou, J. Liu, X. Zhang, Y. Jiang, J.S. Hu, L.-J. Wan, *Sci. China Chem.* **57**, 1552 (2014)
63. A.E. Morales, E.S. Mora, U. Pal, *Rev. Mex. Fis.* **53**, 18 (2007)
64. S. Abermann, *Sol. Energy* **94**, 37 (2013)
65. S. Tomblato, CZTS(e) thin films grown by chemical methods for PV application, Ph.D. Thesis, University of Milano-Bicocca, Bicocca, Italy, 2015
66. P.R. Ghediya, T.K. Chaudhuri, *J. Mater. Sci. Mater. Electron.* **26**, 1908 (2015)
67. P. Kush, S.K. Ujjain, N.C. Mehra, P. Jha, R.K. Sharma, S. Deka, *ChemPhysChem* **14**, 2793 (2013)
68. P.A. Fernandes, P.M.P. Salome, A.F. Cunha, *J. Alloys Compd.* **509**, 7600 (2011)
69. D. Dumcenco, Y.-S. Huang, *Opt. Mater.* **35**, 419 (2013)
70. J. Tauc, R. Grigorovici, A. Vancu, *Phys. Status Solidi (b)* **15**, 627 (1966)
71. P.R. Ghediya, T.K. Chaudhuri, *AIP Conf. Proc.* **1665**, 120032 (2015)
72. D. Tiwari, T.K. Chaudhuri, A. Ray, K.D. Tiwari, *Thin Solid Films* **551**, 42 (2014)
73. V. Kosyak, N.B. Mortazavi Amiri, A.V. Postnikov, M.A. Scarpulla, *J. Appl. Phys.* **114**, 124501 (2013)
74. X. Lin, J. Kavalakkatt, M.C. Lux-Steiner, A. Ennaoui, *Adv. Sci.* **2**, 1500028 (2015)
75. F. Jiang, S. Ikeda, T. Harada, M. Matsumura, *Adv. Energy Mater.* **4**, 1301381 (2014)
76. T.P. Dhakal, C.-Y. Peng, R. Reid Tobias, R. Dasharathy, C.R. Westgate, *Sol. Energy* **100**, 23 (2014)

77. Z. Su, K. Sun, Z. Han, H. Cui, F. Liu, Y. Lai, J. Li, X. Hao, Y. Liu, M.A. Green, *J. Mater. Chem. A* **2**, 500 (2014)
78. W. Wu, Y. Cao, J.V. Caspar, Q. Guo, L.K. Johnson, I. Malajovich, H. David Rosenfeld, K.R. Choudhury, *J. Mater. Chem. C* **2**, 3777 (2014)
79. H. Xin, J.K. Katahara, I.L. Braly, H.W. Hillhouse, *Adv. Energy Mater.* **4**, 1301823 (2014)
80. G. Larramona, S. Bourdais, A. Jacob, C. Choné, T. Muto, Y. Cuccaro, B. Delatouche, C. Moisan, D. Péré, G. Dennler, *J. Phys. Chem. Lett.* **5**, 3763 (2014)
81. C.K. Miskin, W.-C. Yang, C.J. Hages, N.J. Carter, C.S. Joglekar, E.A. Stach, R. Agrawal, *Prog. Photovolt. Res. Appl.* **23**, 654 (2015)
82. G. Brammertz, M. Buffière, S. Oueslati, H. ElAnzeery, K. Ben Messaoud, S. Sahayaraj, C. Köble, M. Meuris, J. Poortmans, *Appl. Phys. Lett.* **103**, 163904 (2013)
83. B. Shin, Y. Zhu, N. Bojarczuk, S.J. Chey, S. Guha, *Appl. Phys. Lett.* **101**, 053903 (2012)
84. I. Repins, C. Beall, N. Vora, C. DeHart, D. Kuciauskas, P. Dippo, B. To, J. Mann, W.C. Hsu, A. Goodrich, R. Noufi, *Sol. Energy Mater. Sol. Cells* **101**, 154 (2012)
85. W. Yang, H.-S. Duan, B. Bob, H. Zhou, B. Lei, C.-H. Chung, S.-H. Li, W.W. Hou, Y. Yang, *Adv. Mater.* **24**, 6323 (2012)